



LAWRENCE  
LIVERMORE  
NATIONAL  
LABORATORY

# Energy Harvesting - An Integrated View of Materials, Devices and Applications

H. B. Radousky, H. Liang

February 1, 2012

Nanotechnology

## **Disclaimer**

---

This document was prepared as an account of work sponsored by an agency of the United States government. Neither the United States government nor Lawrence Livermore National Security, LLC, nor any of their employees makes any warranty, expressed or implied, or assumes any legal liability or responsibility for the accuracy, completeness, or usefulness of any information, apparatus, product, or process disclosed, or represents that its use would not infringe privately owned rights. Reference herein to any specific commercial product, process, or service by trade name, trademark, manufacturer, or otherwise does not necessarily constitute or imply its endorsement, recommendation, or favoring by the United States government or Lawrence Livermore National Security, LLC. The views and opinions of authors expressed herein do not necessarily state or reflect those of the United States government or Lawrence Livermore National Security, LLC, and shall not be used for advertising or product endorsement purposes.

## NANOTECHONOLGY - TOPICAL REVIEW

### Energy Harvesting – An Integrated View of Materials, Devices and Applications

**H. B. Radousky<sup>1\*</sup> and H. Liang<sup>2</sup>**

<sup>1</sup>Lawrence Livermore National Laboratory, Livermore, CA 94578, USA

Department of Physics, University of California-Davis, Davis, CA 95616 USA

<sup>2</sup> Materials Science and Mechanical Engineering, Texas A&M University, College Station, TX, 77843-3123, USA

\* E-mail: radousky1@llnl.gov

#### **Abstract**

Energy harvesting refers to the set of processes by which useful energy is captured from waste, environmental, or mechanical sources and is converted to a usable form. The discipline of energy harvesting is a broad topic that includes established methods and materials such as photovoltaics and thermoelectrics, as well as more recent technologies that convert mechanical energy, magnetic energy, and waste heat to electricity. This article will review various state-of-the-art materials and devices for direct energy conversion and in particular will include multistep energy conversion approaches. The article will highlight the nano-materials science underlying energy harvesting principles and devices, but also include more traditional bulk processes and devices as appropriate and synergistic. Emphasis is placed on device-design innovations that lead to higher efficiency energy harvesting or conversion technologies ranging from the cm/mm scale down to MEMS/NEMS (micro- and nano-electromechanical systems) devices. Theoretical studies are reviewed that address transport properties, crystal chemistry, thermodynamic analysis, energy transfer, system efficiency, and device operation. New developments in experimental methods; device design and fabrication; nanostructured materials fabrication; materials properties; and device performance measurement techniques are discussed.

---

#### **Table of Contents**

- 1. Introduction
- 2. Thermoelectric Materials
  - 2.1 Overview
  - 2.2 ZT for Thermoelectric Materials
  - 2.3 Structures
    - 2.3a Oxides and Silicides
    - 2.3b Half-Heusler compounds
    - 2.3c Skutterudite Materials
    - 2.3d Clathrate Materials
  - 2.4 Properties
    - 2.4a Thermal Conductivity
    - 2.4b Fermi Surface
    - 2.4c Morphology

|    |   |
|----|---|
|    | 2.5 Nano-materials                                  |
|    | 2.6 Applications                                    |
| 3. | Photovoltaic Materials                              |
|    | 3.1 Overview  |
|    | 3.2 Structures                                      |
|    | 3.3 Optical Properties                              |
|    | 3.4 Devices   |
|    | 3.5 Nano-materials                                  |
| 4. | Mechanical Energy Harvesting                        |
|    | 4.1 Overview  |
|    | 4.2 Device Design                                   |
|    | 4.3 Nanomaterials                                   |
|    | 4.4 Pb Free Materials                               |
| 5. | Magnetic Energy Harvesting                          |
|    | 5.1 Overview  |
|    | 5.2 Magnetic/Mechanical Devices                     |
|    | 5.3 Magnetic Materials                              |
| 6. | Combined Energy Harvesting Techniques               |
|    | 6.1 Overview  |
|    | 6.2 Nanodevices                                     |
|    | 6.3 Vibration Energy Transfer                       |
|    | 6.4 Solar Thermoelectric                            |
| 7. | Modeling of Energy Harvesting Devices and Materials |
|    | 7.1 Overview  |
|    | 7.2 Band Structure                                  |
|    | 7.3 Modeling Charge Transfer                        |
|    | 7.4 Modeling Thermoelectric Properties              |
|    | 7.4a Modeling Thermoelectric Efficiency             |
|    | 7.4b Modeling Thermoelectric Generators             |
|    | 7.4c Modeling ZT                                    |
|    | 7.4d Modeling Solar Thermoelectric Systems          |
|    | 7.5 Modeling Nanostructures                         |
|    | 7.6 Modeling Mechanical Energy Harvesting           |
| 8. | Nano-materials in Energy harvesting                 |
| 9. | Conclusion  |
|    | Acknowledgments                                     |
|    | References  |



## 1. Introduction

Energy harvesting is a very broad topic, whose importance in our world is ever increasing. The field is rapidly advancing, and the need for renewable energy, energy efficiency, and energy harvesting is motivating the discovery of new materials and design of new devices. One interesting point is that there is no uniform definition for energy harvesting. It encompasses fields such as solar and thermoelectrics which are well known, as well as many others such as mechanical and electromagnetic harvesting which are less known. There is also the issue of micro vs. macro energy harvesting. You can say that a solar-thermal power plant is doing energy harvesting, but that type of macro-scale use of resources is not covered in this article.

What we have tried to accomplish in this work is to capture a snapshot of the technologies which are emerging as a unified field to capture and reuse energy which traditionally has been wasted. In particular we have focused on those devices and materials which emphasize the use of nano-materials, but have felt free to include any research which fits this broad theme. We specifically have excluded any discussion about the storage and economic issues, which is beyond the scope of this review.

A problem in setting out to review an expanding field is that any one topic could be an entire review article on its own. There are of course many fine review articles on thermoelectrics and solar energy.<sup>1 2 3 4</sup> In order to focus on energy harvesting as an integrated area of research, we have used recent symposiums organized by the authors to help give structure and direction to the topics included here. This review is certainly not inclusive, and we have tried to mention a variety of work which both gives a flavor of the direction of current research, and which emphasizes the emerging overlaps between different aspects of energy harvesting. The reference list will be more extensive than what can be described in the text. The review is divided into the areas of thermoelectrics, photovoltaics, mechanical harvesting, magnetic harvesting, multimode harvesting techniques, modeling of energy harvesting materials and devices. Each of these sections starts with an overview and also contains a sub-section commenting on the role of nano-material to this area of research. Before concluding, we also include a crosscutting section summarizing the increasingly important role of nano-materials in the integrated field of energy harvesting. These sections are briefly described below.

The area of thermoelectric energy harvesting includes thermoelectric materials and devices, as well as applications in automotive waste heat recovery and in some military systems. There have been a number of recent papers on the enhancement of the figure of merit (ZT) of thermoelectric materials area in the last decade.<sup>1 5 6 7 8 9 10</sup> The work in this area is motivated by the possibility of using energy harvesting to reduce the use of fossil fuels. The section on photovoltaic and the general field of solar energy harvesting discusses ideas from the fundamental science of photon processes to the technology of broadband anti-reflective coatings and multi-functional fiber solar cells. There is also a discussion of concentration cells for small scale energy harvesting based on reverse electro-dialysis.<sup>11</sup> The section on Mechanical Energy Harvesting spans the wide range of topics which this type of energy harvesting encompasses.<sup>12 13</sup> Piezoelectrics are involved in devices which harvest wind at the larger scale and potentially could harvest energy from human motion as the smaller scale.<sup>14</sup> New devices which combine piezoelectric with other energy harvesting modes such as magnetic harvesting are expected to play increasingly important roles in the near future.

The need for renewable energy, energy efficiency, and energy harvesting is motivating the discovery of new materials and design of new device structures. A significant number of reports have been published in nanostructured thermoelectric materials. Nanostructured composite

materials are not only promising for thermoelectric, but also in photovoltaics.<sup>15 16</sup> Nanocomposite materials can enhance the thermal-to-electrical power conversion efficiency. One example was the introduction of phase change materials (PCM), which were prepared by compositing exfoliated graphite nanoplatelets (xGnP) into paraffin wax.<sup>17</sup>

The role of new materials in energy harvesting cuts across all of the sub-fields represented here. The need for this enhanced understanding will grow increasingly important as the role of nano-structured materials is enhanced. This review emphasizes the importance of considering energy harvesting as a cross-cutting discipline. Each of the sub-fields represented by the topic headings is important to an understanding of advances across the field as a whole.

## 2. Thermoelectric materials

### 2.1 Overview

Thermal electric (TE) materials have attracted a great deal of attention in recent years due to their wide use in various applications. The thermoelectric effect converts between thermal and electrical energy, and this is illustrated using Figure 2.1-1. Two materials, one n and one p type are connected to the heat source and sink. Electrons are transferred due to different temperatures, resulting in an electrical potential. Conversely, a temperature difference can be induced when a potential is applied.<sup>18 19</sup> A recent focus has been on the improvements of TE efficiency by reducing the lattice thermal conductivity.<sup>9</sup> The reduction can be accomplished by introducing nanostructures or compositing with various microstructures and additives.<sup>4 10 11 18 19 20 21 22 23 24 25</sup>

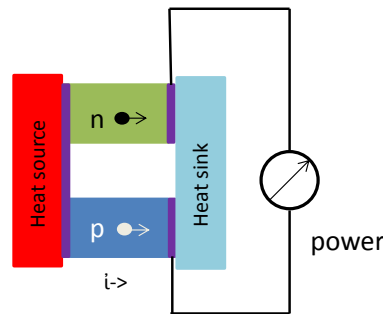


Figure 2.1-1. Illustration of one standard configuration for the thermoelectric effect.

### 2.2 ZT for Thermoelectric Materials

Thermoelectric materials are characterized by the figure of merit  $Z$ .

$$Z = \frac{S^2 \sigma}{k}$$

where  $S$  is the thermoelectric power or Seebeck coefficient,  $k$  is the thermal conductivity, and the electrical conductivity. A dimensionless number  $ZT$  is often used as a figure of merit for the TE material. For conventional materials the  $ZT=1$  at  $T=300K$ .<sup>26</sup> The higher the  $ZT$ , the more efficient the TE.

In order to maximize  $ZT$ , the donor concentration needs to be optimized. Near the Fermi level, a dopant could increase the density of states (DOS), improving the thermopower. When the donor or the acceptor level is near the Fermi level (2.2-1a), the localized DOS is increased, leading to a net increase in the carrier effective mass, without a significant change in the carrier concentration. This increased effective mass results in an improvement in thermopower. For example, the  $ZT$  in TI-doped PbTe was observed to strongly increase, as shown in Fig. 2.2-1b. The net effect was a significant increase in  $ZT$  in comparison with using a dopant which does not have a suitably located energy level.<sup>1 27 28</sup>

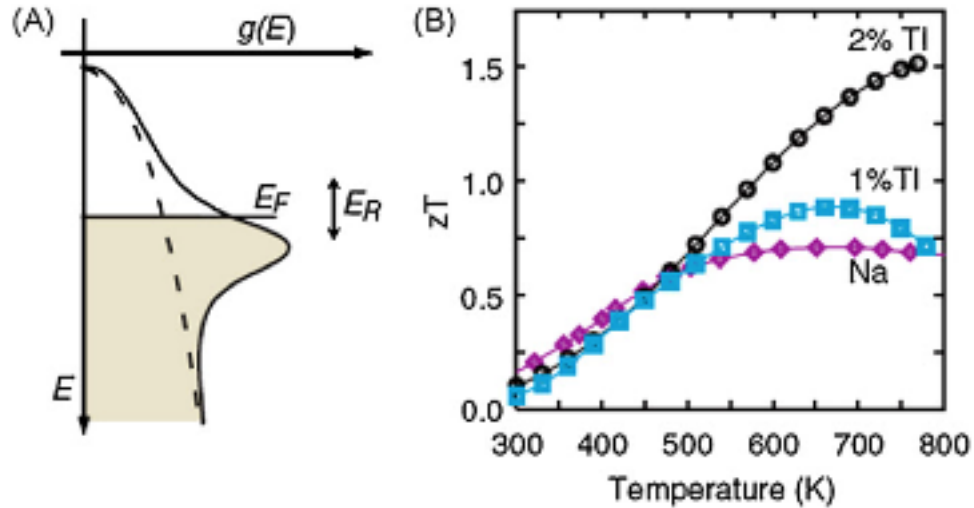


Figure 2.2-1, (a) There is a peak in the density of the state as a solid line is higher than that of the bulk value as dash line. The peak is due to the resonant states in TI-doped PbTe. (b) The measured  $ZT$  on TI-PbTe and Na-PbTe samples for 300-800 k indicates an improvement due to the addition of TI. (From Szczech et al.,<sup>1 27</sup> originally from Heremans et al.<sup>28</sup>)

Figure 2.2-2 shows the  $ZT$  for the Skutterudites  $\text{CoSb}_3$  with multiple co-fillers of Ba, La, and Yb where a high thermoelectric figure of merit  $ZT = 1.7$  was achieved.<sup>18</sup> These results indicate that high power factors can be realized by adjusting the total filling fraction of fillers with different charge states to reach the optimum carrier density, and at the same time reduce the lattice thermal conductivity. The idea of combining multiple fillers with different charge states and rattling frequencies for raising  $ZT$  is also expected to be valid for other caged TE compounds as well.

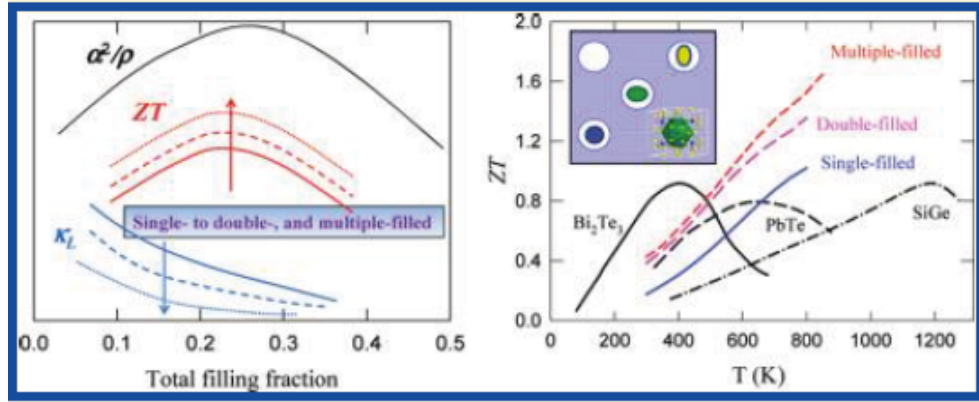


Figure 2.2-2. Skutterudites  $\text{CoSb}_3$  with multiple cofillers Ba, La, and Yb. High power factors can be realized by adjusting the total filling fraction of fillers with different charge states to reach the optimum carrier density. Shi et al.<sup>18</sup>

Some examples of  $Z$  vs Temperature is shown in Figures 2.2-3 and 2.2-4. In the report of Kim et al.,<sup>21</sup> they controlled the grain size on the nano-scale of  $\text{Bi}_2\text{Te}_{2.85}\text{Se}_{0.15}$  as well as the Bi content through the Bi precursor. The effects of this on  $ZT$  are shown in the left side graph in Figure 2.2-3. The right side graph in Figure 2.2-3 shows the  $ZT$  results from Santhanam et al.<sup>29</sup> for the addition of Bi nanocrystals to  $\text{Bi}_2\text{Te}_3$ . Figure 2-2-4 shows the  $ZT$  values for a hydrothermal nanoparticle-plating technique used to grow a layer of  $\text{CoSb}_3$  nanoparticles on the surface of  $\text{La}_{0.9}\text{CoFe}_3\text{Sb}_{12}$  bulk matrix grains. The nanoparticles have a size of 30–40 nm and the nano-layer is hundreds of nanometer thick. A  $ZT$  value near 0.5 is attained at 725 K on the sample with 5 wt % of nanoparticles, giving a 15% improvement of the  $ZT$  from that of the sample without nanoparticles.

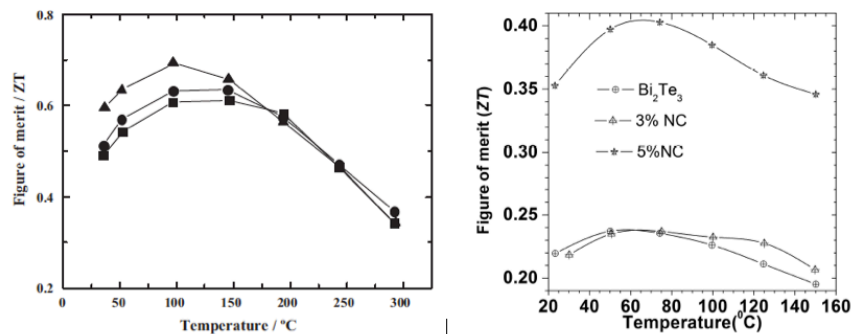


Figure 2.2-3. Left) Temperature dependence of the figure of merit of the specimens prepared with different molar ratios of  $\text{Bi}(\text{NO}_3)_3$ : 2.0 (**Square**), 2.1 (**Circle**), 2.3 (**Triangle**). Kim et al.<sup>21</sup> Right) thermoelectric figure of merit in inclusion-free  $\text{Bi}_2\text{Te}_3$  and  $\text{Bi}_2\text{Te}_3$  with incorporated Bi nanocrystals (NC). Santhanam et al.<sup>29</sup>

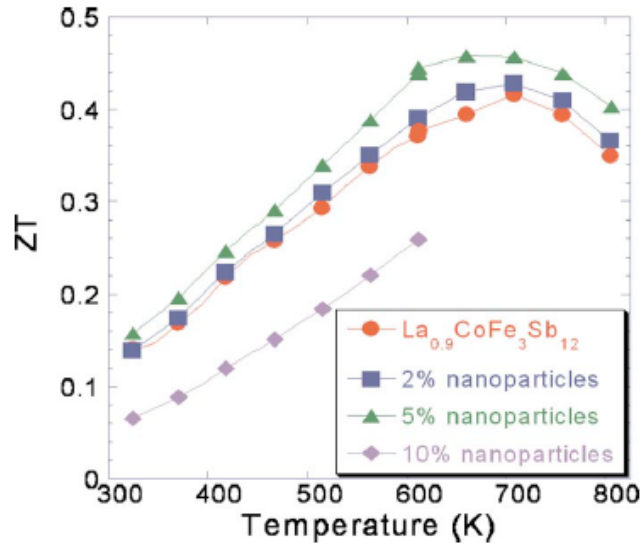


Figure 2.2-4 ZT from 10 to 825 K of the 0%, 2%, 5%, and 10% samples Alboni et. al. <sup>23</sup>

With the objective of increasing the efficiency of thermoelectric materials, attempts have been made to increase the ZT value. For most recently developed materials, however, the figure of merit (FOM) has been less than 2.<sup>30</sup> It has long been recognized that new materials are key to improving the FOM. Figures 2.2-5 and 2.2-6 summarize many of the materials reported to date.

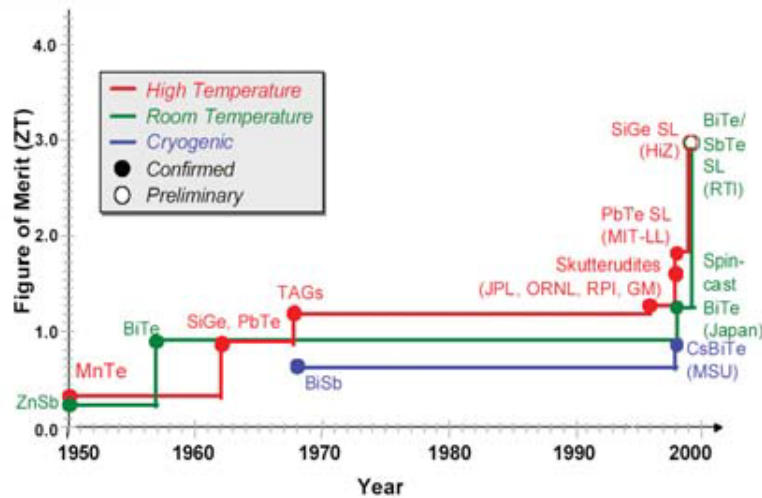


Figure 2.2-5, the Figure of Merit of TE materials developed to date. Choi et al. <sup>30</sup>

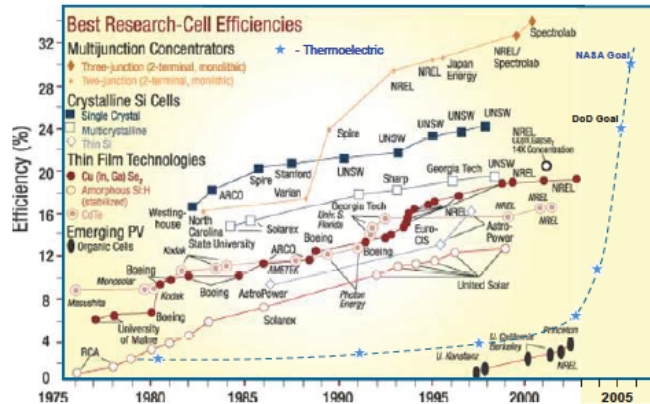


Figure 2.2-6, A list of reported TE and solar materials and their efficiency. Choi et al. <sup>30</sup>

### 2.3 Structures

Alternative TE materials such as hybrid and oxides have also emerged in recent years.<sup>2</sup> Oxides in general are poor choices for TEs due to their low carrier mobility as well as high lattice thermal conductivity. Hybrid and layered structures have been found to be promising TE materials. Figure 2.3-1 compares various materials as TEs. In this figure, the oxides have high chemical and thermal stabilities allowing a high temperature gradient. Figure 2.3-1b lists a few potential nontoxic elements to form oxides. Beside oxides, there are other emerging TE materials and structures reported.<sup>3 7 8 11</sup>

Efforts have been made in developing new materials in order to reduce the thermal conductivity more than the electrical conductivity, and to increase the Seebeck coefficient.<sup>31 32 33 34</sup> The properties of such materials have been investigated against the effects of temperature and models were developed in order to predict their durability and efficiency.<sup>35 36 37</sup> Santhanam et al. report that the inclusion of semimetal nanoparticles into  $\text{Bi}_2\text{Te}_3$  results in an enhancement of the power factor along with a decrease in the lattice thermal conductivity. In particular, the addition of 5%wt nano-inclusions results in a significant increase in the ZT figure of merit, see Figure 2.2-3 in the previous section. The significant increase is attributed to an increase in the electrical conductivity without a corresponding decrease in the Seebeck coefficient.<sup>29</sup>

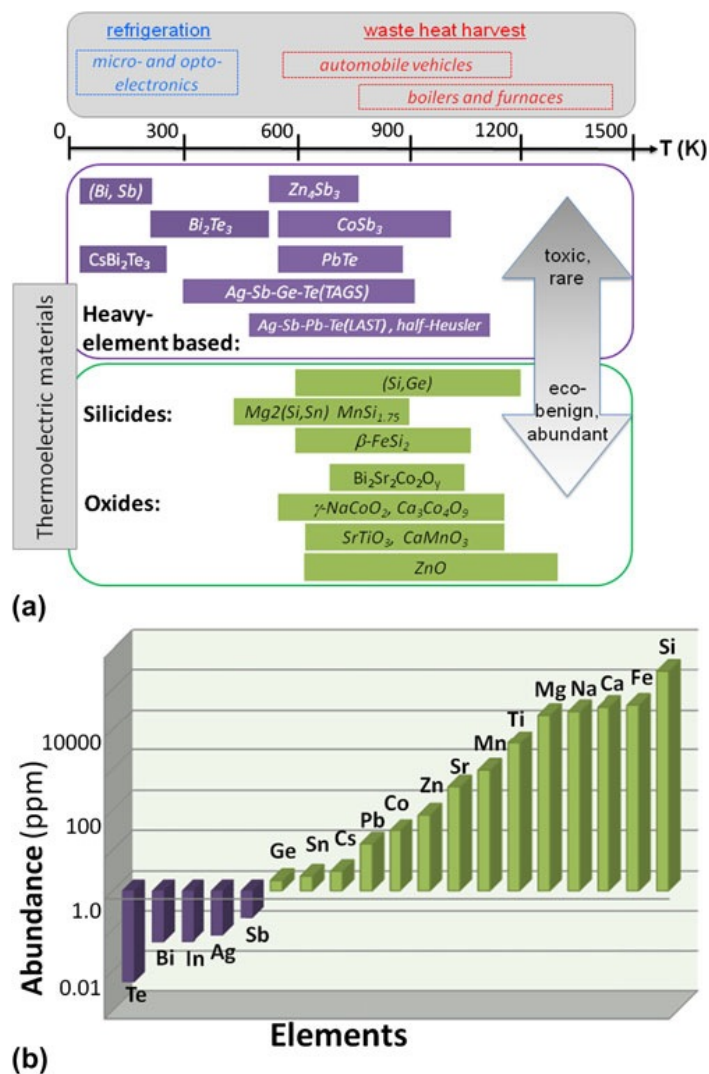


Figure 2.3-1. Summary of existing elements and compounds used as thermoelectric materials. He et al.<sup>2</sup>

### 2.3a Oxides and Silicides

The homologous series of Magnéli phase titanium oxides  $\text{Ti}_n\text{O}_{2n-1}$  ( $n = 2, 3, \dots$ ) have been reported to decrease the thermal conductivity with increasing oxygen deficiency by more than 60% at room temperature and 40% at 773K as compared to  $\text{TiO}_2$ . The largest thermoelectric figure of merit  $Z$ ,  $1.6 \times 10^{-4} \text{ K}^{-1}$  at 773K, was obtained in  $\text{TiO}_{1.90}$  hot pressed specimen.<sup>38</sup>

Magnesium silicide ( $\text{Mg}_2\text{Si}$ ) has been identified as a promising advanced thermoelectric material operating in the temperature range from 500 to 800 K. Compared with other thermoelectric materials that operate in the same conversion temperature range, such as  $\text{PbTe}$ , TAGS (Ge-Te-Ag-Sb) and  $\text{CoSb}_3$ ,  $\text{Mg}_2\text{Si}$  shows interesting aspects, such as the abundance of its constituent elements in the earth's crust and the non-toxicity of its processing by-products.<sup>39</sup> The thermoelectric properties may also be improved in other silicides such as the chimney-ladder compounds in the Ru-Mn-Si System by introducing a high density compositional interface.<sup>15 40</sup>



### 2.3b Half-Heusler compounds

It was reported that the  $(\text{Pb}_{0.95}\text{Sn}_{0.05}\text{Te})_{1-x}(\text{PbS})_x$  nanostructure from nucleation and growth and spinodal decomposition were found to enhance the thermoelectric figure of merit over bulk PbTe, producing a ZT of 1.1 - 1.4 at 650 K for  $x = 0.08$ .<sup>41</sup> The thermoelectric properties have been reported to be improved using half-Heusler compounds  $\text{MnNiSn}$  ( $\text{M} = \text{Ti}, \text{Zr}, \text{Hf}$ ), phase equilibria in the  $(\text{Ti},\text{M})\text{NiSn}$  systems.<sup>42</sup>

These are seen in Figure 2.3-1 back scattered electron images. The  $(\text{Ti}_{0.4}\text{Zr}_{0.6})\text{NiSn}$  and  $(\text{Ti}_{0.4}\text{Hf}_{0.6})\text{NiSn}$  shown here were treated via different methods. The phase constitution of each alloy varies depending on the difference in its solidification path and phase equilibrium. The solubility of solid solutions is labeled in Figure 2.3-1.<sup>42</sup>

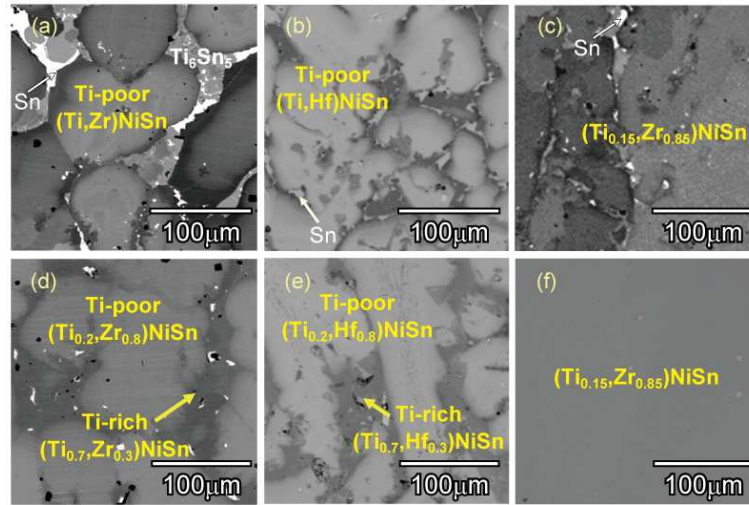


Figure 2.3-1, Images of back scattered electrons of microstructures of  $(\text{Ti}_{0.4}\text{Zr}_{0.6})\text{NiSn}$  (a,d),  $(\text{Ti}_{0.4}\text{Hf}_{0.6})\text{NiSn}$  (b,e), and  $(\text{Ti}_{0.15}\text{Zr}_{0.85})\text{NiSn}$  (c,f) alloys. (a-c) was samples of arc-melt as-casted, (d,e) are samples annealed for 336h, and (f) was directly solidified as-grown. Kenjo et al.<sup>42</sup>

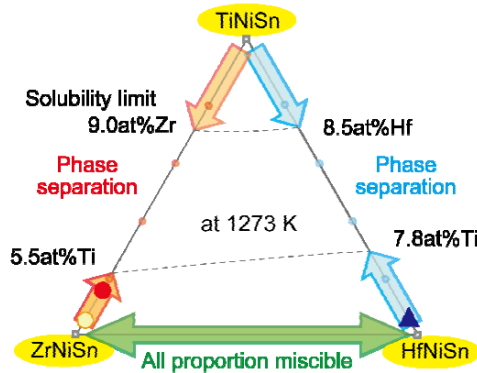


Figure 2.3a-2, Illustration of the solubility limits in  $\text{TiNiSn}$  and  $(\text{Zr},\text{Hf})\text{NiSn}$  solid solutions. Circles and triangle show chemical compositions of nearly single-phase alloys prepared for thermoelectric properties. Kenjo et al.<sup>42</sup>



### 2.3c Skutterudite Materials

Materials with complex crystal structures and large unit cell constants can have Phonon-Glass-Electron Crystal (PGEC) structures.<sup>1 4 15 27</sup> As shown in Figure 2.3c-1a, the compounds, such as  $\text{Yb}_{14}\text{MnSb}_{11}$  are a promising example of such a system. They contain a valence balanced combination of cations and covalently bonded anionic units. The combination of covalent and ionic bonding can lead to higher charge mobilities than purely ionic compounds and large, complex unit cells with intrinsically low thermal conductivity.  $\text{Yb}_{14}\text{MnSb}_{11}$  is an excellent material for high temperature thermoelectrics having reported ZT of 1.0 at 1223 K and up to 1.3 with optimized alloying. Nowotny chimney ladder<sup>15 40</sup> (NCL) compounds (Fig. 2.3c-1b) are another class of complex crystal structure materials which are promising as PGECs. They have a variable length, columnar sublattice of non-metal atoms (ladders) residing in the channels (chimneys) of a metal atom sublattice, forming homologous families of complex structures with variable unit cell length or incommensurate crystal structures.

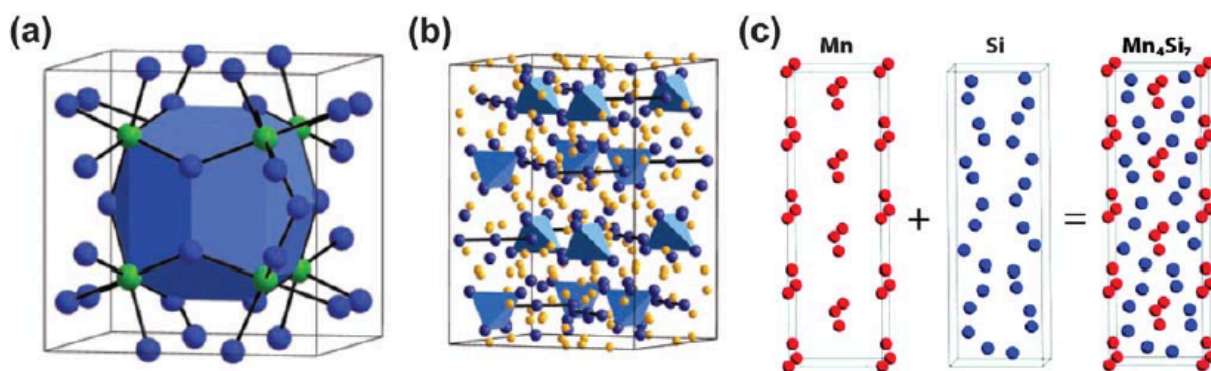


Figure 2.3c-1 (a) The crystal structure of the skutterudite compound  $\text{CoSb}_3$ , showing the formation of large void spaces (blue polygon) formed by the arrangement of tilted octahedra of Co (green) and Sb (dark blue). (b) The structure of the Zintl compound  $\text{Yb}_{14}\text{MnSb}_{11}$ , consisting of  $[\text{Sb}_3]^{7-}$  trimmers (dark blue),  $[\text{MnSb}_4]^{2-}$  tetrahedra (turquoise), isolated Sb atoms (dark blue), and the  $\text{Yb}^{2+}$  sublattice (yellow). (c) A model of NCL structures, using  $\text{Mn}_4\text{Si}_7$  as an example, showing the formation of the complex crystal structure from Mn and Si sublattices. From Szczech et al.,<sup>1</sup> originally from G. J. Snyder et al.<sup>4</sup> and Higgins et al.<sup>27</sup>

### 2.3d Clathrate Materials

Recent improvements in thermoelectric efficiency appear to be dominated by a reduction in the lattice thermal conductivity. This reduction is accomplished by the careful introduction of 0.1–5 nm sized “objects” that effectively scatter acoustic phonons without significantly affecting electronic transport.<sup>9</sup> Compounds with cage-like structures, such as the clathrates or skutterudites (discussed in the previous section), use atoms which can rattle in their cage to lower the lattice thermal conductivity. In the clathrate compound shown in Figure 2.3d-1, the Ba ions are weakly bound at the center of a large polyhedron. The low-frequency optical phonon modes hybridize with the acoustic phonons (which carry most of the heat) and produce a lower thermal conductivity. In general, the scattering of acoustic phonons by atoms rattling in a cage is more effective in reducing the lattice thermal conductivity than effects produced from substitutional alloying.

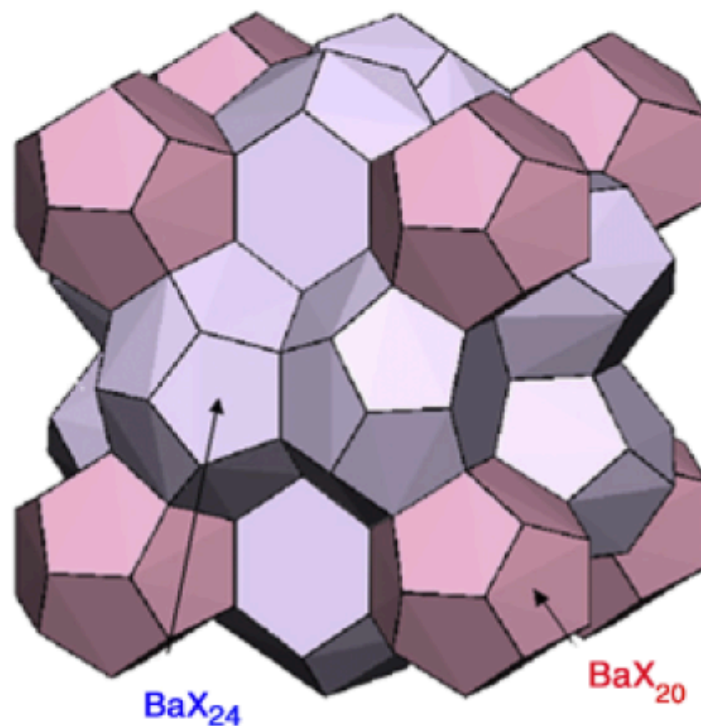


Figure 2.3d-1. Schematic of the type I clathrate compound  $\text{Ba}_8\text{Ga}_{16}\text{Ge}_{30}$ . The Ba ions are located near the center of each polyhedron with 24 (blue) or 20 (red) vertices. X refers to either Ga or Ge. Sales<sup>9</sup>

## 2.4 Properties

The inclusion of nanoparticles is thought to reduce the thermal conductivity in thermoelectric materials. Vineis<sup>19</sup> discuss how the inclusion of nanodots can reduce the thermal conductivity below the alloy limit. Detailed calculations of phonon transport have been performed for  $\text{ErAs}:\text{InGaAs}$  materials.<sup>43</sup> Atomic scale defects in alloys can scatter phonons due to differences in their mass or due to a generation of strain fields, and the scattering cross-section follows Rayleigh scattering. This implies that short wavelength phonons are effectively scattered in alloys, but the longer wavelength phonons can propagate without causing significant scattering and will contribute to heat conduction.

Thermal conductivity values of nanostructures such as superlattices can also be significantly lower than that of their bulk constituent materials.<sup>23 44</sup> The reduction in thermal conductivity can lead to a large increase in the thermoelectric figure of merit in superlattice systems. Superlattices grown by thin-film deposition techniques, however, are not suitable for large scale applications. Nanocomposites represent a different approach that can lead to high thermoelectric figure merit.<sup>45</sup>

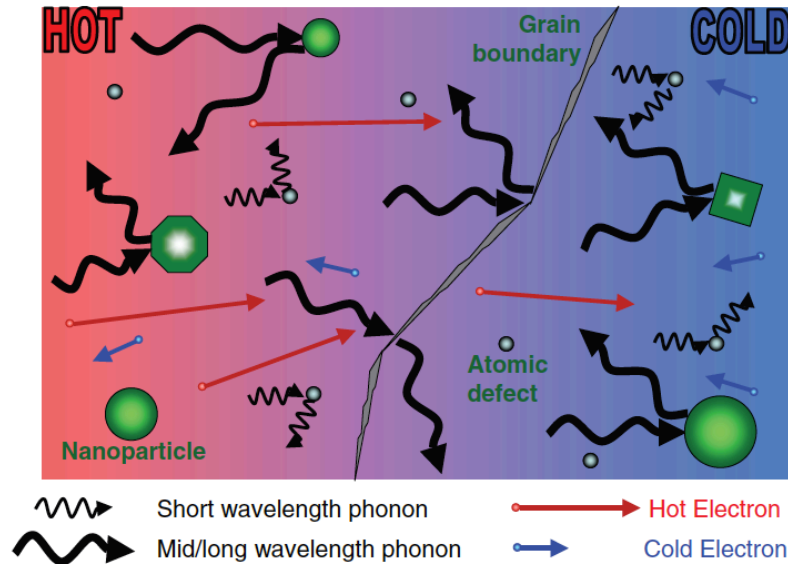


Figure 2.4-1, Schematic diagram illustrating various phonon scattering mechanisms with a thermoelectric material, along with electronic transport of hot and cold electrons. Atomic defects are effective at scattering short wavelength phonons, but larger embedded nanoparticles are required to scatter mid- and long-wavelength phonons effectively. Grain boundaries can also play an effective role in scattering these longer-wavelength phonons. Vineis et al.<sup>19</sup>

Figure 2.4-2 shows the different components which contribute to the thermopower. Maximizing the efficiency ( $ZT$ ) of a thermoelectric involves a compromise of thermal conductivity and Seebeck coefficient with the electrical conductivity. Trends shown were modeled from  $\text{Bi}_2\text{Te}_3$ . The interdependence of the thermopower, electrical conductivity, and thermal conductivity can be clearly seen.<sup>1 20</sup>

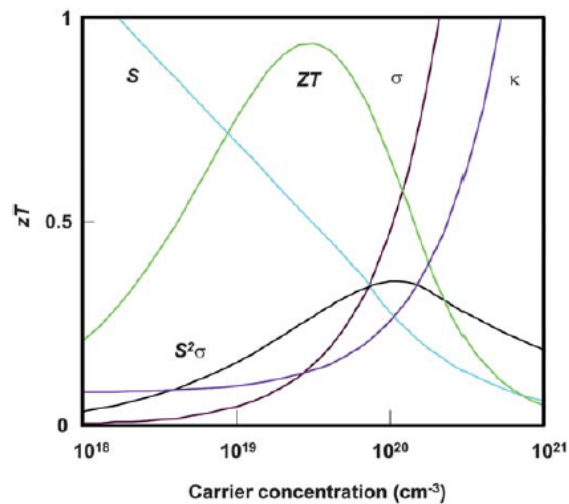


Figure 2.4-2 Interdependence of the thermopower ( $S$ ), electrical conductivity ( $\sigma$ ), and thermal conductivity ( $\kappa$ ). From Szczec<sup>1</sup>, originally from Snyder<sup>20</sup>

## 2.4a Thermal Conductivity

One critical question to explore with the addition of nanomaterials is what part of the reduction in thermal conductivity in these thermoelectric materials can be directly linked to additions of nanoparticulates such as nanodots. This is a non-trivial question since these systems typically have other coexisting defects—including solid-solution behavior—that are known to inhibit heat flow. Figure 2.4a-1 shows a comparison of lattice thermal conductivities for five PbTe-based materials systems plus pure PbTe. This figure shows that while solid-solution point defect scattering alone is effective in lowering the lattice conductivity of PbTe by  $\sim 30\text{-}40\%$ , nanostructuring contributes additional phonon scattering for an overall 75% reduction. <sup>19</sup>

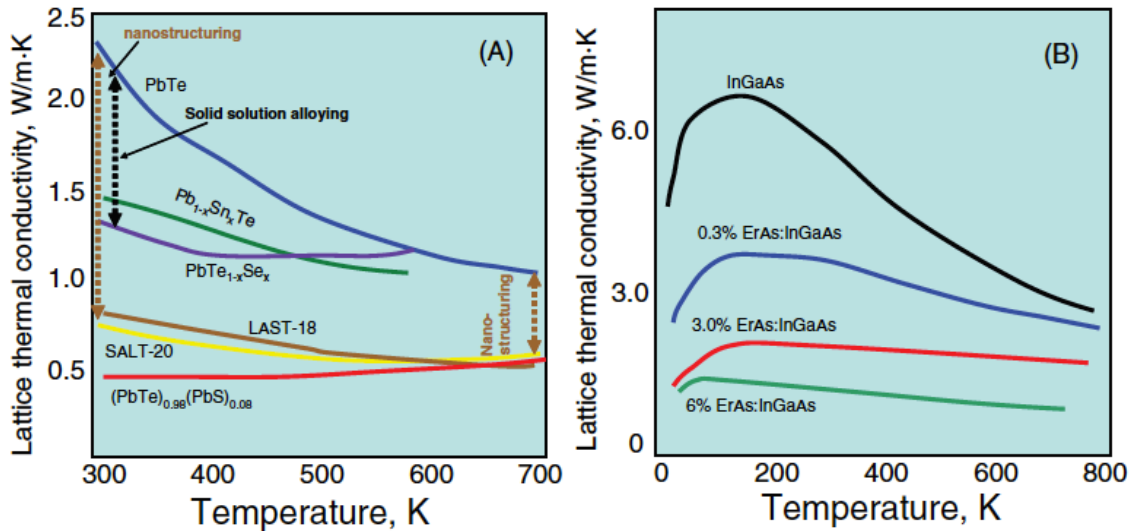


Figure 2.4a-1, Lattice thermal conductivity as a function of temperature for: (a) various PbTe-based alloys ( $x = 0.1$ ) and nanostructured samples. The value of  $x = 0.1$  was chosen because these samples have the same concentration of added component to PbTe as those in LAST-18 and SALT-20. (b) InGaAs with and without embedded ErAs nanodots. It is seen in both cases that the inclusion of nanodots in the microstructure results in a significant reduction to the lattice thermal conductivity. In the PbTe system solid solution alloying is effective around room temperature (black dotted arrow) but not at high temperature. Nanostructure is shown to be effective both at room temperature and at high temperatures (brown dotted arrows). Vineis et al.<sup>19</sup>

ErAs:InGaAs is another interesting example to study along these lines since the size distribution of ErAs nanoparticles in the matrix is not a strong function of the growth parameters and they are typically 2–4 nm in diameter. The volume fraction of the embedded nanoparticles can be modified from 0.01–6% without introducing defects or dislocations. Figure 2.4a-2 shows the thermal conductivity measurements are reduced by as much as a factor of 3 compared to the bulk alloy. <sup>43</sup>

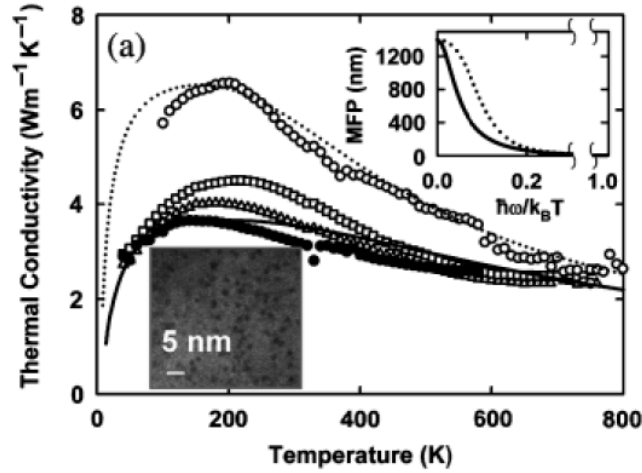


Figure 2.4a-2 Thermal conductivity of randomly distributed epitaxial ErAs nanocrystals (solid circles) in an  $\text{In}_{0.53}\text{Ga}_{0.47}\text{As}$  alloy is also shown as open circle. (Kim et al.)<sup>43</sup>

## 2.4b Fermi Surface

Understanding the galvanomagnetic and thermoelectric properties including the Hall effect, electrical resistivity, thermopower, and thermal conductivity all depend on characterization of the electronic properties. The electronic band structure, density of states, dispersion curves, and Fermi surface were calculated by Candolfi et al.<sup>6</sup> for the  $\text{Ba}_8\text{Ni}_x\text{Si}_{46-x}$  for  $x=4$  materials within the full-potential local-orbital method (FPLO). Their calculations show that density of states at the Fermi level strongly varies with  $x$ . The variations in the band structure have been experimentally confirmed by transport properties and specific heat measurements. Regardless of the Ni content, the Fermi surface, shown in Figure 2.4b-1 presents disconnected electron and hole sections that appear consistent with thermopower data, where both types of carriers contribute to the electrical conduction in these materials. All the samples they modeled exhibited metallic-like behavior causing moderate thermopower values for ZT.

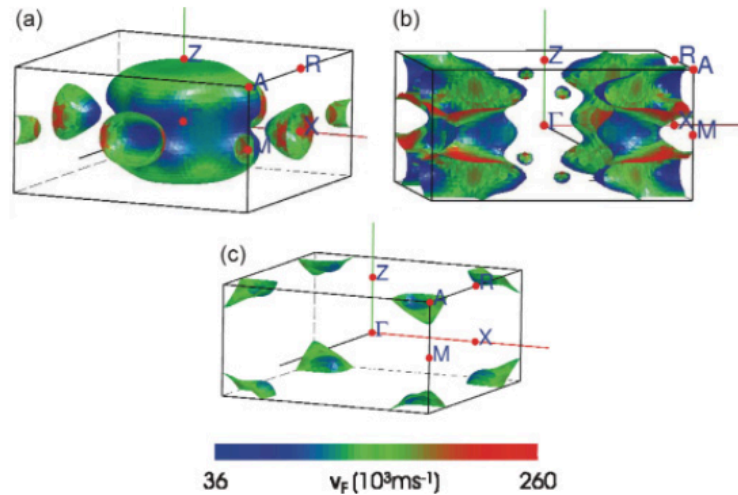


Figure 2.4b-1, Fermi surface of  $\text{Ba}_8\text{Ni}_x\text{Si}_{46-x}$  for  $x=4$ . The shading is by Fermi velocity. Candolfi et al.<sup>6</sup>

## 2.4c Morphology

Nanostructured materials are often polycrystalline and can be used to control interfaces in order to enhance the thermal electric properties.<sup>4</sup> The approaches in controlling microstructures and interfaces are illustrated in Fig. 2.4c-1. It includes preferentially aligning the grains for transport directions (Fig. 2.4c-1b), grain size reduction (Fig. 2.4c-1c), forming thin layers of a second phase at the boundaries (Fig. 2.4c-1d), embedding nanoinclusions in grains (Fig. 2.4c-1e), and producing plate or lamellar nanostructures (Fig. 2.4c-1f).

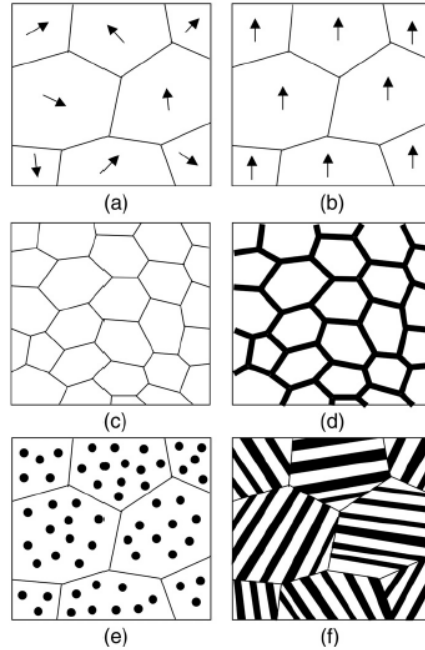


Figure 2.4c-1. Improving bulk thermoelectric performance employs several distinct classes of grain and interfacial microstructure. (a) A polycrystalline microstructure. (b) Preferential alignment of grains along favorable transport directions. (c) Reduced grain size to take advantage of favorable interfacial scattering processes. (d-f) Nanocomposites: (d) nanocoated grains. (e) embedded nanoinclusions, and (f) laminar/multilayer structures. Medlin et al.<sup>4</sup>

## 2.5 Nanomaterials for Thermoelectrics

Many papers reported the use of nanomaterials in thermoelectric materials, with a good overview given by Pichanusakorn and Bandaru.<sup>46</sup> Vaquero and Powell<sup>7</sup> discussed using nanoscale precipitates within a matrix for the pseudo-binary system  $(\text{AgSbTe}_2)_x(\text{PbTe})_{1-x}$ . This system is considerably more complex than the solid-solution behavior. Partial substitution of lead by a mixture of silver and antimony produce phases which depends on the lead content,  $x$ . Examination using transmission electron microscopy reveals the presence of (Ag, Sb)-rich nanoinclusions within a PbTe rocksalt matrix as shown in Figure 2.5-1. The nanoinclusions are thought to scatter acoustic phonons with minimal scattering of charge carriers, which results in a high figures of merit,  $ZT = 1.7$  at 700 K.

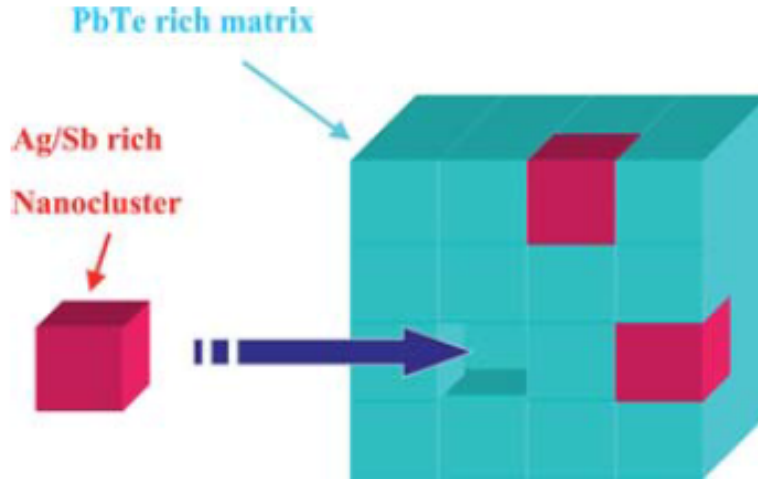


Figure 2.5-1, A schematic representation of the nanostructure of the  $\text{Ag}_{1-x}\text{Pb}_m\text{SbTe}_{m+2}$  phases. Vaqueiro and Powell<sup>7</sup>

The possibility of enhanced ZT in aligned homogeneous porous structures, as shown in Figure 2.5-2, has been discussed by Yang et al.<sup>1 47</sup> For a composite with a given porosity, the thermal conductivity is expected to decrease as the pore radius decreases and interface density increases. This is shown in Figure 2.5-2 b. For optimum pore wall thickness and pore periodicity, a seven-fold enhancement of the power factor is predicted, with more modest enhancements expected as the pore radius and periodicity deviate from their optimum values.

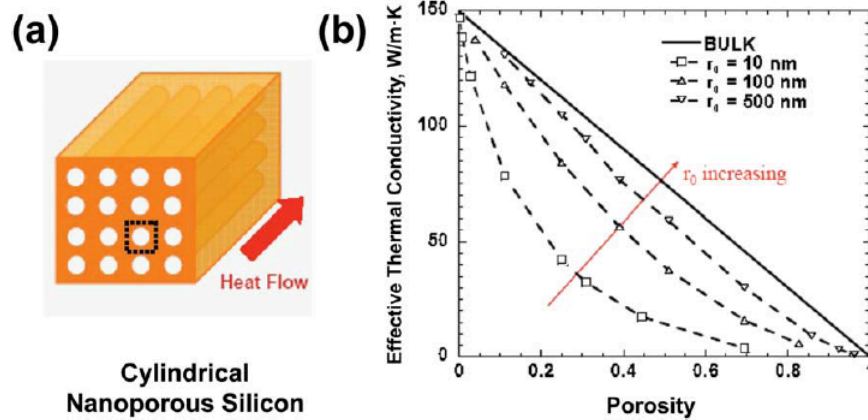


Figure 2.5-2, Nanoporous silicon with aligned cylindrical pores, with heat transport in the direction of the pore axis. (b) Effective thermal conductivity as a function of porosity with different radii. Szczec et al.,<sup>1</sup> originally from Yang et al.<sup>47</sup>.

Figure 2.5-3 shows the minimum confinement length ( $a_{\min}$ ) for improved properties in select thermoelectric materials. Pichanusakorn and Bandaru<sup>10</sup> have shown that there exists a threshold confinement length only below which lower dimensional nanostructures, such as QWs or



NWs, could have a higher power factor compared to bulk materials. For example, Si NWs with diameter below 4 nm would be required for an enhanced power factor over bulk values.

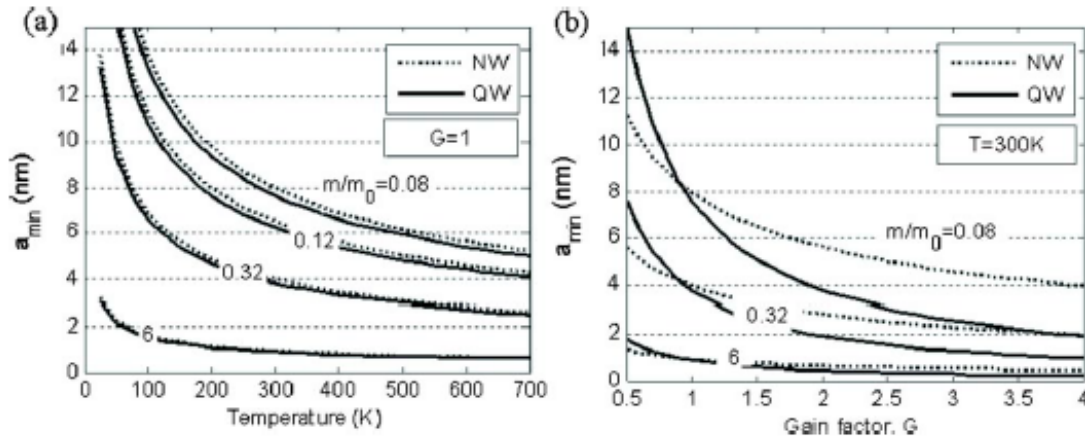


Figure 2.5-3 (a) The minimum confinement length ( $a_{\min}$ ) for select thermoelectric materials, at which one-dimensional NWs (dotted lines) and two-dimensional QWs (solid) have a greater  $S^2\sigma$  compared to bulk thermoelectrics (the gain factor,  $G=1$ ). (b) The  $a_{\min}$  as a function of  $G$  for NWs and QWs, decreases much faster for the latter at higher  $G$ . Pichanusakorn and Bandaru<sup>10</sup>

Yadav et al.<sup>24</sup> have studied the thermoelectric properties of quantum dot (QD) nanocomposites in which the QDs are aligned to form chains. In both the InAs/GaAs and Ge/Si systems, they use a constant relaxation time approximation to calculate and compare the electrical conductivity, Seebeck coefficient, and thermoelectric power factor for QD chains, three-dimensional ordered QD arrays, random QD arrays, and bulk GaAs or Si. Figure 2.5-5 illustrates the alignment of QDs, which can take place either parallel to the growth direction, vertical chain or perpendicular to the growth direction, and horizontal chain. In the directions perpendicular to the QD chain, 2D confinement is approximated by two 1D QWs with confined subband energy levels. An effective potential  $V_{\text{eff}}$  along the QD chain can be calculated, as illustrated in Figure 2.5-5. This  $V_{\text{eff}}$  is then used in a Kronig–Penny model to calculate the miniband energy levels as a function of  $kx$ , i.e., the miniband dispersion  $E_{kx}$ . Finally,  $E_{kx}$  is used to calculate the density of states,  $2/L_y L_z dk_x / dE$ . The electronic transport properties are then calculated using the Boltzmann transport equations summed over all  $n$  minibands.



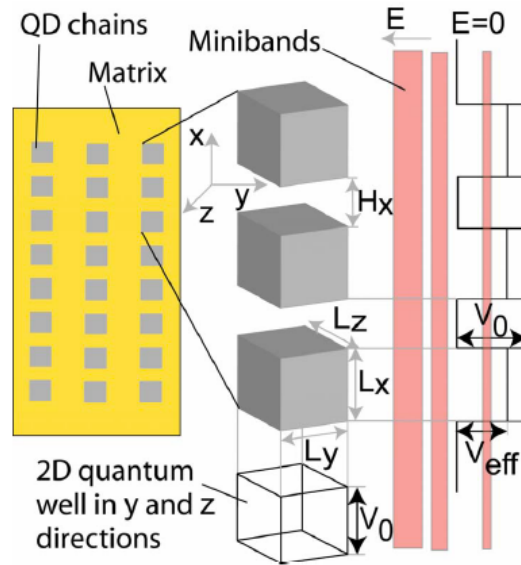


Figure 2.5-5 Illustration of aligned quantum dot chain, energy minibands, and potential wells in the  $x$ ,  $y$ , and  $z$  direction.  $L_x$ ,  $L_y$ , and  $L_z$  are the QD sizes in the same directions,  $H_x$  is the QD spacing along the direction of alignment,  $V_0$  is the confining potential, and  $V_{\text{eff}}$  is the effective confining potential for the  $x$  direction. Yadav et al.<sup>24</sup>

Figure 2.5-6 summarizes a comparison between bulk and nanostructured composite materials. Szczech et al.<sup>1</sup> discusses that the last decade of research resulted in the discovery of new bulk materials with better thermoelectric performance and the development of nanoscale and nanostructured materials have independently achieved ZT above 1.5.

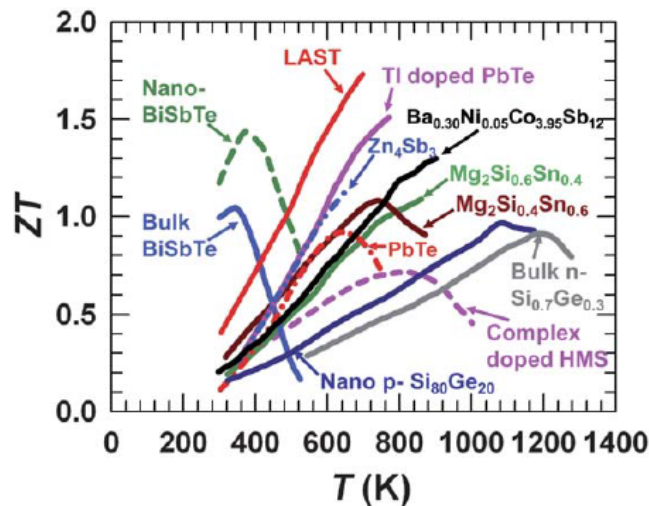


Figure 2.5-6 State-of-the-art comparison of ZT in conventional bulk materials and nanostructured composite materials. From Szczech et al. <sup>1</sup>, originally courtesy of Prof. Li Shi (U Texas–Austin).

## 2.6 Applications

Pichanusakorn and Bandaru discuss the applications which could arise from a jump in efficiency of thermoelectric materials to nanoscale engineering.<sup>10</sup> The problem of waste heat recovery, e.g., from transportation vehicles and oil refineries along with heat dissipation, e.g., in microelectronics – where leakage currents in transistors exponentially increase with temperature, is of considerable relevance to energy generation and conservation. While the basic principles underlying these processes are well known, the use of these materials is not very widespread due to low efficiency. Thermal to electrical energy conversion, through thermoelectric and thermionic materials, has been proposed to be much more efficient in lower dimensional materials at the nanoscale. If nanostructured thermoelectrics could be practically implemented, such an approach could be of wide practical import. For example, mechanical cycle-based systems could be replaced by solid state based thermoelectric structures with advantages such as components with no moving parts along with a rapid response time. A brief glimpse of the possibilities is illustrated in Figure 2.6-1.<sup>46</sup>

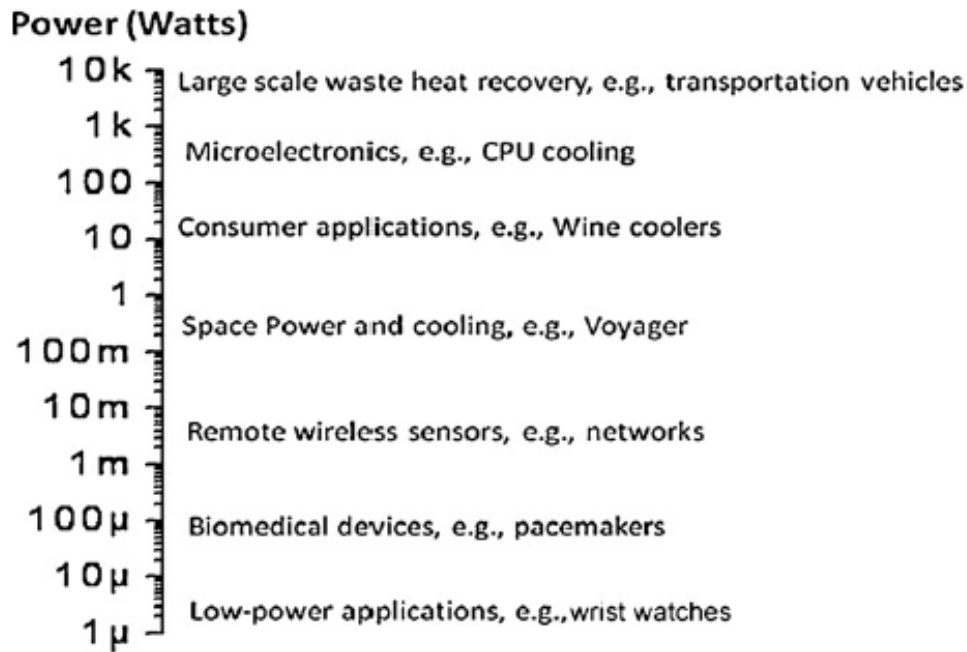


Figure 2.6-1, thermoelectric materials can be put to use in various energy conversion applications, encompassing ten orders of magnitude in power. Pichanusakorn et al.<sup>46</sup>

### 3. Photovoltaic Materials

#### 3.1 Overview

Photovoltaics (PV) involves converting solar radiation into electrical energy through semiconductor materials. Solar energy harvesting involves transferring light into electricity through certain types of chemical reaction.<sup>48</sup> The energy production usually starts with the light being absorbed by assembled molecules. Subsequently, electrons are excited and transferred to an acceptor. The most common materials used today are amorphous silicon, single crystal silicon, polycrystal silicon, cadmium telluride, copper indium gallium selenide, and copper indium gallium sulfide.<sup>49</sup> There are a wide variety of nanomaterials used as solar materials for energy harvesting. Those include nanotubes,<sup>50</sup> quantum dots,<sup>51 52 53</sup> nanocrystals,<sup>54</sup> among others. The advancement of nanoparticle synthesis in well-defined geometrical shapes could result in innovative design for solar energy conversion.

Kamat et al discuss three possible approaches to design solar energy conversion devices (Figure 3.1-2).<sup>55</sup> The figure on the left is designed to mimic photosynthesis, with donor-acceptor molecular assemblies and clusters. The second (middle) is showing semiconductor assisted photocatalysis to produce fuels such as hydrogen. The third on the right is using nanostructures as semiconductor based solar cells.<sup>56</sup>

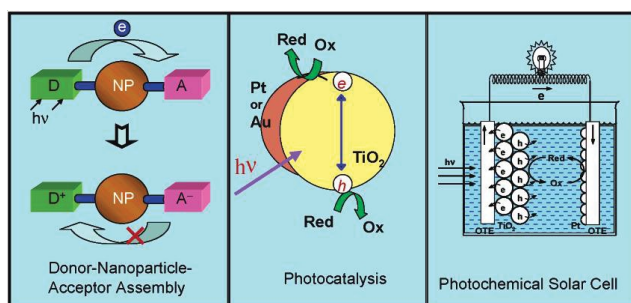


Figure 3.1-1, shows three strategies to use nanostructures for solar energy conversion. The first step is the nanoparticle assembly, second is photocatalysis, and third the photochemical solar cells. Kamat et al.<sup>55</sup>

Solar thermoelectric power generation is rapidly becoming cost competitive for utility scale electricity. Parabolic trough concentrators have proven economical and reliable but their efficiency is limited by the maximum temperature of the heated fluid. The solar thermoelectric trough collector is an option, not a good application for a  $ZT=1$  thermoelectric material. To increase the overall power output of the system by approximately 10% would require a  $ZT=3$  material.<sup>57</sup> An intermediate-band material based on thiospinel semiconductor  $MgIn_2S_4$  was reported as a high efficiency photovoltaic material for intermediate-band solar cells.<sup>58</sup> Other materials have been reported with similar effects.<sup>59 60 61</sup>

#### 3.2 Structures

Channon et al.<sup>56</sup> discuss the fluorescence characteristics of a system where the light harvesting occurs in fibrils. Two precursors were chosen to promote resonance energy transfer (RET) following self-assembly, as shown in Figure 3.2-1. In a binary system, excitation of donor

species should result in rapid transfer of excitation energy to acceptor sites and observation of emission from acceptors (Figure 3.2-1, bottom). The starting mixture comprises a large excess of donor species to facilitate energy migration from excited donors to red-shifted traps (the acceptor species). If the donor and acceptor have comparable lifetimes, then in the time required for the acceptor to relax from the excited state, most of the donors will also have relaxed, releasing the harvested energy.

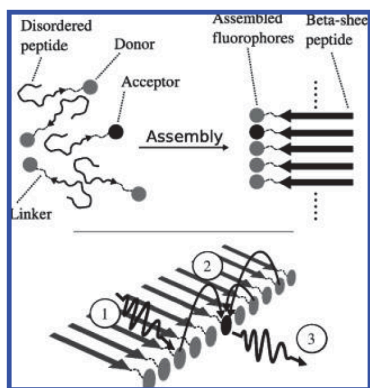


Figure 3.2-1, Each synthetic precursor comprises a peptide component (arrow) and organic fluorophore (disk). Two types of precursors were synthesized: donors (gray disks) and acceptors (black disks). Donors and acceptors are mixed and self-assembled to form a fiber (right). (Bottom) Light harvesting occurs in fibrils via (1) absorption of a photon by the donor and (2) nonemissive transfer to an acceptor via RET. The energy is released by the acceptor as an observed photo (3), allowing confirmation of light harvesting in the system. Channon et al.<sup>56</sup>

### 3.3 Optical Properties

Small peptides offer an attractive starting point for the development of solar harvesting materials since they are relatively simple to produce and can be tailored to provide an expansive range of chemical functionality.<sup>56</sup> One route is the use of biological molecules to drive the self-organization of chromophores to perform a light-harvesting function analogous to that of the light-harvesting complexes (LHCs) that enable efficient photosynthesis in bacteria and green plants. The energy transfer behavior of the fibrils (as discussed in the previous section) is shown in Figure 3.2-1. Channon et al.<sup>56</sup> diluted samples 300-fold into H<sub>2</sub>O and transferred to a quartz cuvette for analysis. Excitation of fibrils at the donor absorption maximum (465 nm; Figure 3.2-1 left) resulted in significant emission from the acceptor. Under those conditions, no significant emission from the acceptor was observed upon excitation at the donor excitation maximum (Figure 3.2-1, right). Comparison with modeling results indicates that the acceptors harvest energy from more than one donor.

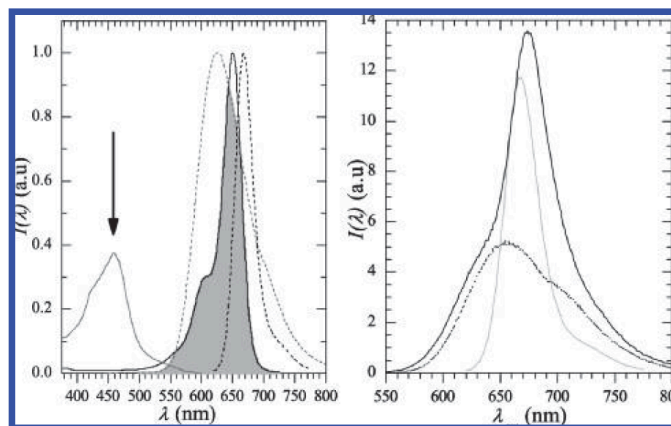


Figure 3.2-1, Fluorescence excitation (solid) and emission (dashed) spectra of RuBiPy (donor, gray) and Alexa 647 (acceptor, black). The arrow indicates the wavelength of excitation used to demonstrate light harvesting in the fiber. The shaded area illustrates the overlap between donor emission and acceptor excitation. (right) Emission spectra of light-harvesting fibrils (solid, black) at 465 nm. Also shown are emission from an equivalent but unincubated mixture of donor and acceptor (dotted, black) and emission from direct excitation of the acceptor (gray) at 645 nm. Channon et al.<sup>56</sup>

Kamat et al. discusses three major ways to utilize nanostructures for the design of solar energy conversion devices: (i) Mimicking photosynthesis with donor-acceptor molecular assemblies or clusters, (ii) semiconductor assisted photocatalysis to produce fuels such as hydrogen, and (iii) nanostructure semiconductor based solar cells.<sup>55</sup> Figure 3.2-2 shows the emission from modified Au nanoparticles linked to a TiO<sub>2</sub> film. Controlled charging of the Au nanoassembly enables the modulation of the excited-state interaction between the gold nanocore and a surface-bound fluorophores. Spectroelectrochemical experiments carried out using a thin layer electrochemical cell showed the emission spectra of pyrene modified gold particles which were linked to TiO<sub>2</sub> film cast on an optically transparent electrode (OTE/TiO<sub>2</sub>/-OOC-R2-S (Au)-S-R1-Py) and subjected to different applied potentials (Figure 3.2-2). The overall shape of the emission band remains the same with changing bias, suggesting that the photoactive molecule contributing to the emission is unperturbed.

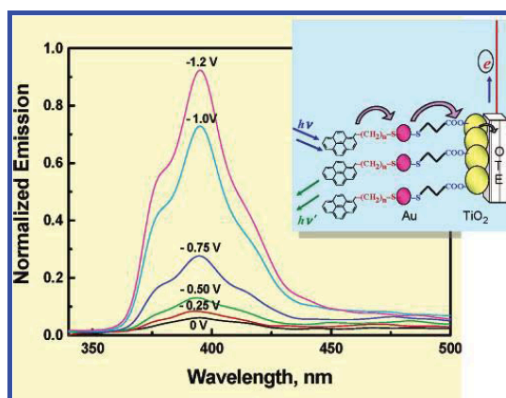


Figure 3.2-2 Modulation of photo induced charge transfer in a pyrene modified gold particles linked to TiO<sub>2</sub> film cast on an optically transparent electrode (OTE). Kamat et al.<sup>55</sup>

Zhang et al.<sup>59</sup> discuss the self-assembly of stable nanoscale coordination polymers (NCPs), which exhibit temperature-controlled guest encapsulation and release, as well as an efficient light-harvesting property. The NCPs are obtained by coordination-directed organization of  $\pi$ -conjugated dicarboxylate (L1) and lanthanide metal ions Gd(III), Eu(III), and Yb(III) in a DMF system. Guest molecules trans-4-styryl-1-methylpyridiniumiodide (D1) and methylene blue (D2) can be encapsulated into NCPs, and the loading amounts can be controlled by changing reaction temperatures. Guest-loaded NCPs exhibit efficient light harvesting with energy transfer from the framework to the guest D1 molecule, which is studied by photoluminescence and fluorescence lifetime decays. Experimental results showed that the guest loading amount increased with an increase of the temperature from 20 to 140 °C. As shown in Figure 3.2-3, by normalizing the absorption peak that resulted from L1, the peak of D1 in NCPs at ~480 nm increased for the sample prepared at 140 °C. This was further supported by the color changes of the samples after purification (Figure 3.2-3, inset).

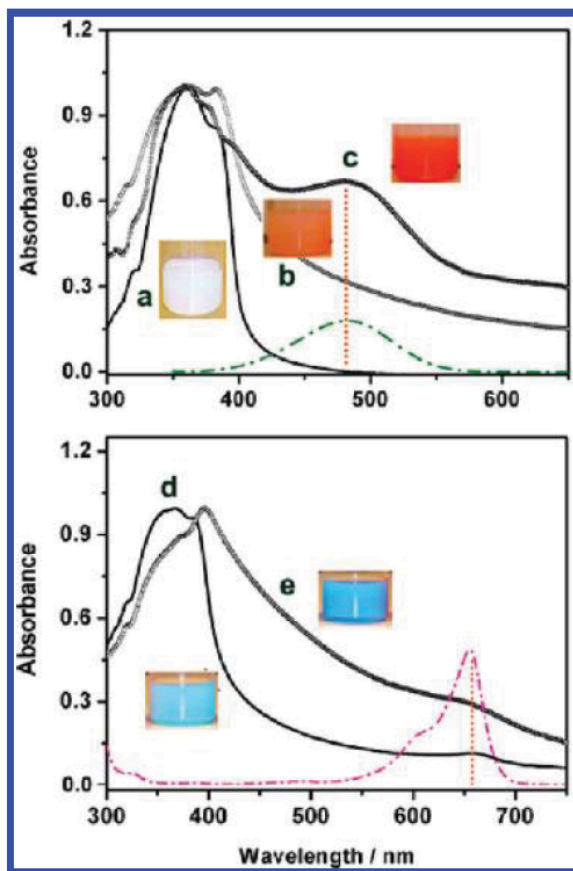


Figure 3.2-3, Normalized UV-vis absorption spectra of NCPs dispersed in ethanol: (a) Gd-L1 prepared at 20 °C; (b) Gd-L1-D1 prepared at 20 °C; (c) Gd-L1-D1 prepared at 104 °C; (d) Gd-L1-D2 prepared at 20 °C; (e) Gd-L1-D2 prepared at 140 °C. The dashed curves are the absorptions of free D1 and D2 in ethanol, respectively. Inset: photograph of the corresponding NCPs dispersed in ethanol. Zhang et al.<sup>59</sup>

### 3.4 Devices

Organic solar arrays can be used in dc power supplies for electrostatic microelectromechanical systems devices.<sup>62</sup> The bulk heterojunction (BHJ) “plastic” solar cell has been developed in recent years for solar energy harvesting. Peet et al.<sup>63</sup> discuss that only 0.1% of the total electricity generated in the United States comes directly from sunlight and point out that the earliest commercial solar technology remains the basis for the most prevalent devices in current use, namely, highly-ordered crystalline, inorganic solar cells. Future progress in the fabrication of high-performance BHJ cells will depend on new processing methods, which control both the BHJ phase separation and the internal order of the components, and can be implemented to increase the power conversion efficiency (PCE). Properly controlling the “nanomorphology”, which is critically dependent on minute experimental details at every step, from synthesis to device construction, provides a possible path to >10%. Another important factor is that PCE BHJ cells, which can be fabricated at a fraction of the cost of conventional solar cells. Figure 3.4-1 shows the results from using a focused ion beam to “cut” cross sections through the BHJ film for characterization via atomic force microscopy (AFM) and transmission electron microscopy (TEM).

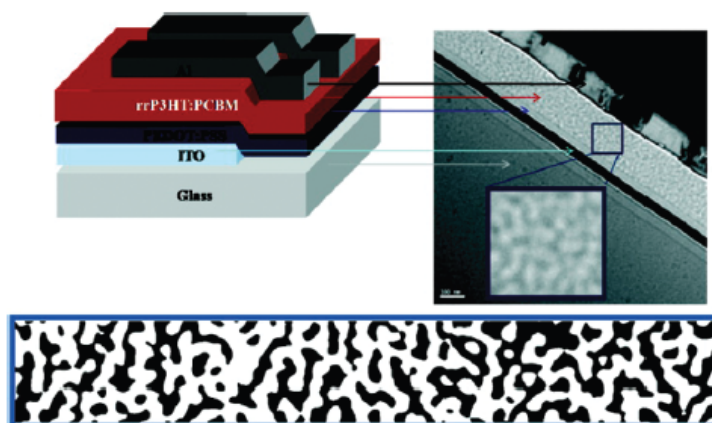


Figure 3.4-1, Cross-sectional TEM of a BHJ solar cell with a contrast-enhanced image to highlight the continuous domains of P3HT and PC61BM. Peet et al.<sup>63</sup>

Lewis et al.<sup>62</sup> discuss an innovative way to fabricate organic solar arrays for application in dc power supplies for electrostatic microelectromechanical systems devices. A solar array with 20 miniature cells interconnected in series was fabricated and photolithography was used to isolate the individual cells, with result shown in Figure 3.4-2. The best performing single cell was fabricated with an active layer thickness of 200 nm followed by a post-device thermal annealing at 120 °C for 5 min.



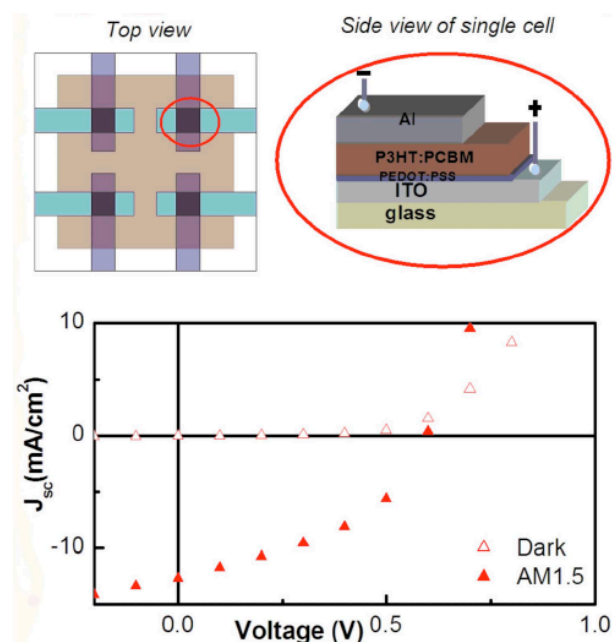


Figure 3.4-2, Upper panel: schematic of a single organic solar cell with bulk heterojunction structure. Lower panel: current-voltage characteristics of single cell made with P3HT:PCBM mixed with weight ratio of 1:1 under simulated AM1.5G, radiation at 132.6 mW/cm<sup>2</sup>. The active layer was spun-coat on patterned ITO substrate at 800 rpm, with a final thickness of about 200 nm. Post-device thermal annealing at 120°C for 5 min was done before the I-V measurements. Lewis et al. <sup>62</sup>

### 3.5 Nano-materials

Liu et al.<sup>64</sup> discuss that the incident-photon-to-current-conversion efficiency of TiO<sub>2</sub> photoanodes can be increased significantly in the visible and near infrared range of the electromagnetic spectrum by assembling films that are structured on both micrometer and nanometer length scales. Photoanodes assembled from alternating layers of TiO<sub>2</sub> nanoparticles and mesoporous TiO<sub>2</sub> microspheres increase the overall power conversion efficiencies of dye-sensitized solar cells by as much as 26%. This increase is attributed to enhanced light scattering by porous TiO<sub>2</sub> microspheres.

During the conversion of the titanium glycolate microspheres to TiO<sub>2</sub>, the hydrolysis and condensation reactions introduce mesopores into the spheres but the particles retain their shape as shown in Figure 3.5-1. Figure 3.5-1 (a) and Figure 3.5-1 (b) show the morphologies of the titanium glycolate and the TiO<sub>2</sub> microspheres obtained after the hydrothermal reaction, respectively. The titanium glycolate spheres are 400–600 nm in diameter and have smooth surfaces. After the hydrothermal reaction, the diameters of the spheres had shrunk slightly to 300–500 nm.



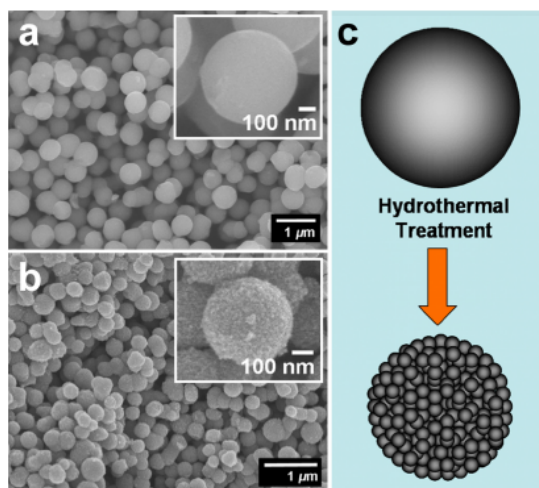


Figure 3.5-1 SEM images of (a) the titanium glycolate precursor microspheres and (b) the porous anatase  $\text{TiO}_2$  microspheres. Insets are high-magnification SEM images showing the surfaces of the microspheres. (c) Schematic illustration of the formation mechanisms of the porous  $\text{TiO}_2$  microspheres. Liu et al.<sup>64</sup>

Layered photoanode structures can enhance light harvesting efficiency by increasing the path lengths of photons through the film via scattering.<sup>64</sup> Example photon paths through a two-layer film are illustrated in 3.5-2. First, back scattering by the microspheres and reflections at the nanocrystal-FTO interface trap photons in the first nanocrystalline (N) layer and increase their path length through the dye coated  $\text{TiO}_2$  nanoparticles (paths 1 and 2 in 3.5-2 ). Second, the photons that are transmitted into the microsphere film are efficiently scattered which also increases their effective path length (paths 3 and 4 in Figure 3.5-2 ). Finally, additional alternating layers on top can capture those photons that have managed to pass through the microsphere layer without absorption (path 5 in Figure 3.5-2 ). Simulations of the Mie scattering by the microspheres show that the scattering efficiency is maximized at wavelengths, 1–1.4 time the particle diameter, implying that microsphere diameters of 300–500 nm are best. Figure 3.5-3, shows a high-resolution SEM image of the alternating four-layered electrode assembly.

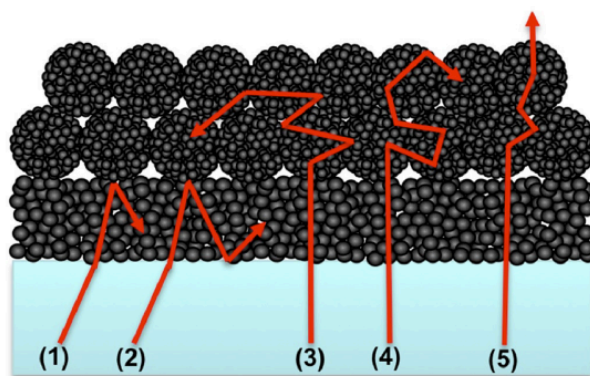


Figure 3.5-2, Schematic illustration of light scattering in an electrode consisting of porous microspheres. Liu et al.<sup>64</sup>

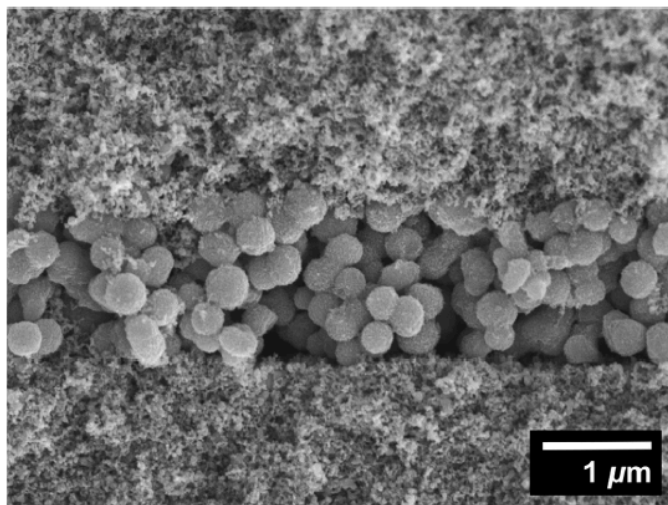


Figure 3.5-3, High-resolution SEM image of alternating four-layered electrode assembled from P25 nanoparticles and porous TiO<sub>2</sub> microspheres. Liu et al.<sup>64</sup>

Organized inorganic-organic nanohybrids, with hierarchical superiority in architecture, have been developed by assembling monolayers of organic molecules containing functional groups, such as amines, thiols, isothiocyanate, and silanes, on to the three dimensional surface of metal nanoparticles.<sup>55-65</sup> They exhibit efficient light-harvesting capability and suppress undesirable energy transfer quenching of the porphyrin singlet excited-state by the gold surface relative to the bulk gold. Examples of gold nanoparticles functionalized with different ligands are shown in Figure 3.5-4. The optical properties of the functionalized Au nanoparticles was discussed above in Section 3.2.

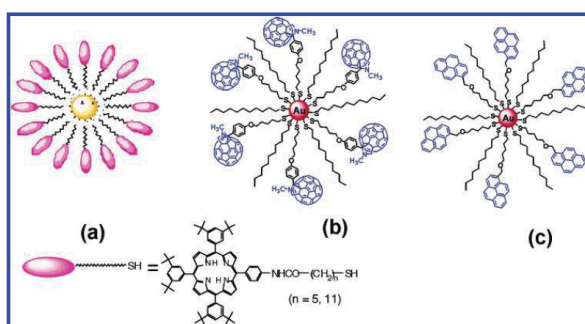


Figure 3.5-4 Examples of gold nanoparticles functionalized with (a) porphyrin, (b) C60, and (c) pyrene (from ref 29) Kamat et al.<sup>55</sup>, originally from Thomas and Kamat.<sup>65</sup>

Zhang et al.<sup>59</sup> show in Figure 3.5-5 NCPs assembled from linear  $\pi$ -conjugated ligand and lanthanide metal ions with long-range ordered structures, which exhibit temperature controlled sizing, guest encapsulation and release, and an efficient light-harvesting property. The lanthanide ions were chosen as metal connectors because of their high affinity to carboxylate and nondetrimental nature to fluorescence. The optical properties of the NCPs were discussed above in Section 3.2.

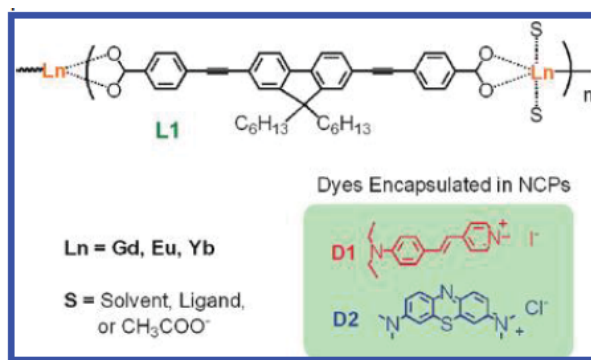


Figure 3.5-5, Molecular structures of ligand L1 and guests encapsulated in NCPs. Zhang et al.<sup>59</sup>

## 4. Mechanical Energy Harvesting

### 4.1 Overview

Mechanical energy is associated with the motion and position of an object. In this review, mechanical energy harvesting involves materials and devices that convert mechanical energy into other types of energy, such as electrical, magnetic, thermal, among others. The most common type of mechanical energy being harvested is mechanical vibration. There are several basic types of harvesting devices based on mechanical vibration.<sup>66</sup> Often, mechanical vibration energy can be harvested using resonant mechanical structures via vibrations.<sup>67 68 69</sup> The scavenged energy is then transformed into electricity by piezoelectric materials. This type of energy conversion can also be enhanced through a magnetic field.<sup>70 71 72</sup> The second type is through change of ambient temperature using a permanent magnet attached to a PZT/brass bimorph, and placed near a "thermo-magnetic" material (FeNi) at which Curie temperature can be tuned around the ambient. Such type of harvesting depends on the slow cooling and heating through ambient air. Another type is the low-frequency, large amplitude bending from human motion using a light, flexible electro-active polymer membrane.<sup>73 74</sup>

### 4.2 Device Design

The design of devices plays important roles in mechanical harvesting efficiency. The structures of materials have been reported to enhance the efficiency of energy conversion.<sup>75 76 77,78</sup> One popular example is to make the piezoelectric polymer into wave shapes, as shown in Figure 4.2-1<sup>79</sup> A wavy piezoelectric ribbon on silicone rubber resulted amplitudes in the waves accommodate order-of-magnitude increases in maximum tensile strain without fracture. The buckled ribbons enhanced the piezoelectric effect of up to 70%, representing the highest reported piezoelectric response on a stretchable medium. These results allow for the integration of energy conversion devices which operate in stretching mode via reversible deformations in the wavy/buckled ribbons.

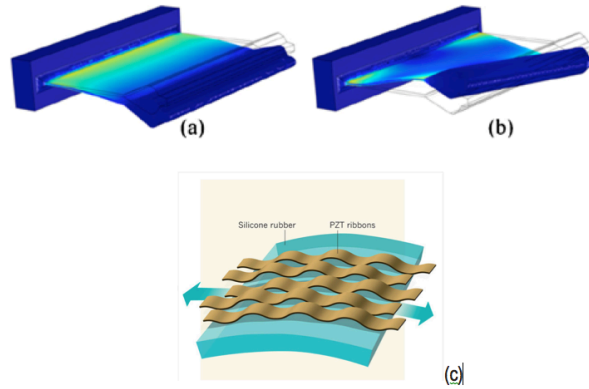


Figure 4.2-1, COMSOL modeled eigenmodes of the energy harvesters main-cantilever, (a) first bending mode at 101.3 Hz, (b) first torsional mode at 315.9 Hz.<sup>88</sup> (c) The stretchable devices consist of wavy ribbons made of piezoelectric material (lead zirconate titanate; PZT) on silicone rubber. Such structure can withstand greater applied mechanical strain without cracking than can equivalent materials made into flat ribbons. Qi et al.<sup>73-79</sup>

It was reported that nanowire radial heterostructures of silicon are the optimal design for efficient charge density. Tian and co-workers<sup>80</sup> synthesized this type of nanowires with p-n and p-i-n radial heterostructures by the VLS mechanism and subsequent thin film deposition and characterized the photovoltaic response of individual nanowires (Figure 4.2-2). The single nanowire photovoltaic device was able to power a logic circuit and a nanowire pH sensor on a self-contained circuit.<sup>80</sup>

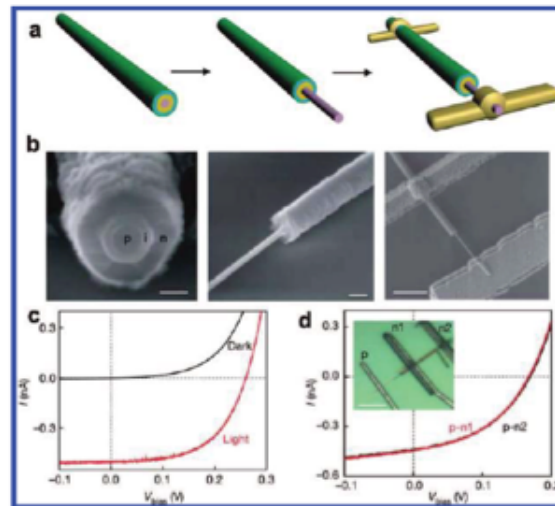


Figure 4.2-2, (a) Schematics of single nanowire PV device fabrication. (left) Pink, yellow, cyan, and green layers correspond to the p-core; i-shell, n-shell, and PECVD-coated SiO<sub>2</sub> respectively. (Middle) Selective etching to expose the p-core. (right) Metal contacts deposited on the p-core and n-shell. (b) SEM images corresponding to schematics in a. Scale bars are 100 nm (left), 200 nm (middle), and 1.5  $\mu$ m (right). (c) Dark and light I-V curves. (d) light I-V curves for two different n-

shell contact locations. (inset) Optical microscopy image of the device. Scale bar, 5  $\mu$ . Hochbaum and Yang.<sup>77</sup>

Great attention has been given in elastic solar materials to mechanically compliant sources of power.<sup>81 82 83 84 85</sup> To harvest mechanical energy through vibration, the mechanical components are desirable to be elastic without deformation nor allow conformal bonding to substrates. One of the main challenges of nano-power components is energy storage. Yu et al., gives an example of a stretchable supercapacitor.<sup>86</sup>

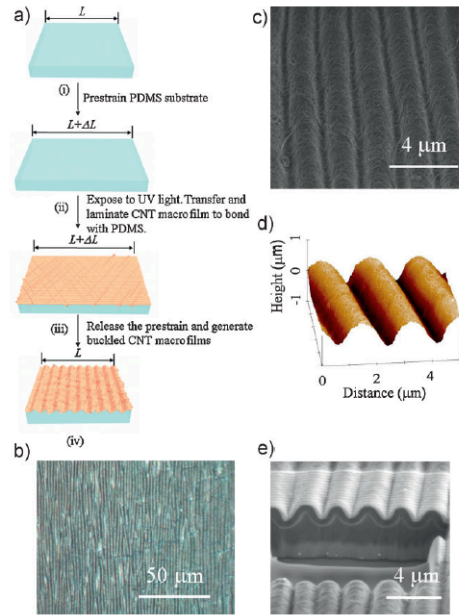


Figure 4.2-3, Fabrication steps of a buckled SWNT macrofilm on an elastomeric PDMS substrate. a) Illustration of the fabrication flow comprising surface treatment, transfer, and relaxation of the prestrained PDMS substrate. b) Optical microscopy image of a 50-nm-thick, buckled SWNT macrofilm on a PDMS substrate with 30% prestrain, where the well-defined periodic buckling structure is shown. c) SEM image of a buckled SWNT macrofilm. The buckling wavelength is 2mm. d) AFM image of the buckling profile of the SWNT macrofilm. The buckling amplitude is 0.4mm. e) SEM image of the buckled SWNT macrofilm/PDMS substrate interface, where the top white layer is a very thin layer of platinum that was sputtered onto the SWNT macrofilm in advance to prevent the SWNT macrofilm from damage during ion milling. Yu et al.<sup>86</sup>

Figure 4.2-4a illustrates F1 5 PZT ribbons (5-10 nm wide and 250-500 nm thick) were patterned on a magnesium oxide (MgO) host substrate and subsequently released from the mother substrate using phosphoric acid (85% concentration, 75 C, 50 s). A slab of PDMS (2mm thick) was then elastically stretched and brought into conformal contact with the ribbons. Peeling off the PDMS allowed for complete transfer of the PZT ribbons to the elastomer via adhesive van der Waals forces in the surface-dominated ribbons. Finally, releasing the prestrain in the PDMS led to



a compressive force in the PZT ribbons as the PDMS relaxed to zero strain, leading to periodic de-adhesion and buckling. The resulting wavy geometry is a result of the transfer of mechanical compressive energy into bending energy. Figure 4.2-4b is a scanning electron microscopy (SEM) image of PZT ribbons transferred using unstrained PDMS. The Figure 4.2-4c shows PZT ribbons with a wavy/buckle structure induced by the prestrained PDMS.

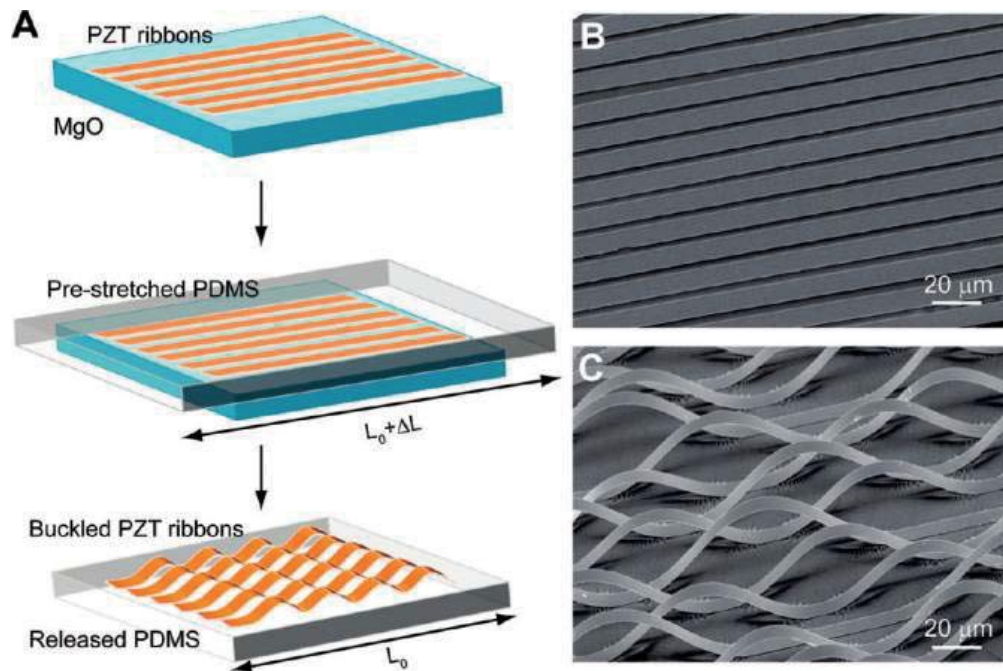


Figure 4.2-4, The wavy/buckled piezoelectric PZT ribbons. (a), (top-down), PZT ribbons were patterned on an MgO substrate and undercut etched to release them from the mother substrate; a slab of pre-strained PDMS was laminated against the ribbons and peeled off quickly; retrieved PZT ribbons were transferred onto PVMS and formed wavy/buckled structures upon strain relaxation. (b) SEM image of PZT ribbons transfer printed to PDMS with zero pre-stain. (c) PZT ribbons spontaneously buckled under pre-strained conditions. Qi et al.<sup>79</sup>

### 4.3 Nanomaterials

Nanomaterials have promising applications as nanogenerators. In particular, PZT nanofibers can be produced through electrospinning, as discussed by Chen et al.<sup>75</sup> PZT nanofibers are deposited on the preprepared interdigitated electrodes of platinum fine wire (diameter of 50 nm) arrays, which were assembled on a silicon substrate (Figure 4.3-1a). The diameters of PZT nanofibers were 60 nm (Figure 4.3-1b) through varying the concentration of poly vinyl pyrrolidone (PVP) in the modified sol-gel solution. A soft and polymer (polydimethylsiloxane, PDMS) was applied on top of the PZT nanofibers (Figure 4.3-1c). The PZT nanofibers were poled by applying an electric field of 4 V/μm across the electrodes (Figure 4.3-1d) at a temperature of above 140 °C for about 24 h. The power generation mechanisms of the nanogenerator are illustrated in Figure 4.3-1d-e. Here the PZT nanofibers worked in the longitudinal mode with an alternating pressure

applied on the top surface of the nanogenerator. The applied pressure was transferred to the PZT nanofibers through the PDMS matrix and resulted in charge generation due to the combined tensile and bending stresses in the PZT nanofibers. A voltage difference between the two adjacent electrodes was thereby induced due to this separation of charge. The interdigitated electrodes could enhance the power output of the nanogenerator. The piezoelectric nanofibers between each pair of adjacent electrodes served as unit cells, and each cell was connected in parallel.<sup>75</sup>

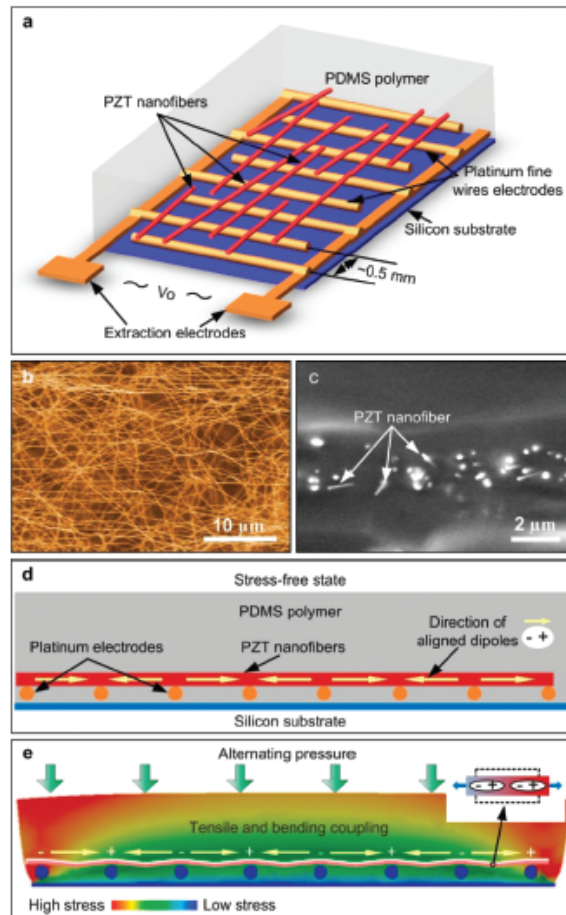


Figure 4.3-1, concept and power generation mechanism of the PZT nanofiber generator. (a) Schematic view of the PZT nanofiber generator. (b) Scanning electron microscopy (SEM) image of the PZT nanofiber mat across the interdigitated electrodes. (c) Cross-sectional SEM image of the PZT nanofibers in the PDMS matrix. (d) Cross-sectional view of the polled PZT nanofiber in the generator. (e) Schematic view explaining the power output mechanism of the PZT nanofibers working in the longitudinal mode. The color presents the stress level in PDMS due to the application of pressure on the top surface. Chen et al.<sup>75</sup>

#### 4.4 Pb Free Materials

The piezoelectric ribbon materials can be made of PZT, PVDF, or other types. The PZT contains lead that might have potential health issues. Rai et al.<sup>87</sup> discuss finding lead-free materials. One example is shown in (Figures 4.2-1 and 4.2-2). Attempts have been made to

produce efficient lead-free piezoelectric materials. Solid solution with composition  $(\text{KNa})\text{NbO}_3-x\text{ABO}_3$ , (where  $A = \text{Li}$ , and  $B = \text{Nb}$ ;  $x = 0, 5, 5.5, 6$ , and  $6.5 \text{ wt\%}$ ) were developed. Single phase formation and good crystallinity with  $\text{LiNbO}_3$  addition up to  $x = 6.5 \text{ wt\%}$  was reported. Dielectric studies reveal that the composition with  $\text{LiNbO}_3 = 6.5 \text{ wt\%}$  exhibits properties suitable for piezoelectric energy harvesting applications.<sup>87</sup>

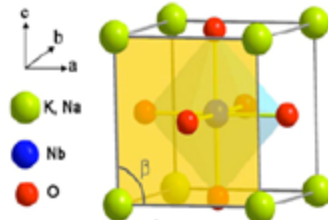


Figure 4.4-1, Crystal structure of KNN. Rai et al.<sup>87</sup>

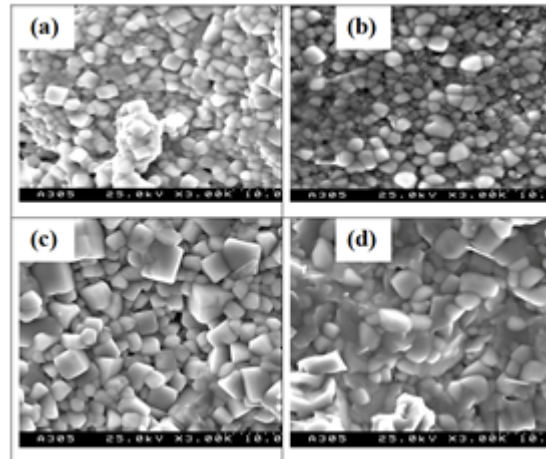


Figure 4.4-2, SEM images of KNN-xLN system with  $x=(a) 5.0$ ,  $(b) 5.5$ ,  $(c) 6.0$ , and  $(d) 6.5$ . Rai et al.<sup>87</sup>

Mechanical energy harvesting can be done through hybrid composite, lead-free materials<sup>87</sup> in linear or non-linear vibration,<sup>88 89 90 91 92</sup> wind energy,<sup>93 94</sup> and locomotion.<sup>95</sup> Efforts have been made on modeling of the efficiency of devices.<sup>96</sup> Figure 4.4-3 shows a PZT nanogenerator which uses a free vibrating PZT cantilever as a damper. The output voltage from the nanogenerator was measured when a Teflon cantilever, placed on top of the nanogenerator, was subjected to free vibration, as shown in Figure 4.4-3b. The damping ratio and the natural frequency of this system were determined to be 0.064 and the 49.9 rad/s (7.9 Hz), respectively. The output voltage from a dummy block without PZT nanofibers or any active materials in it was also measured using the same setup. The measured result revealed that the amplitude of noise signal is only at about 10 mV level. This confirmed that the power output from the PZT nanogenerator was in fact the energy harvested from mechanical vibration.



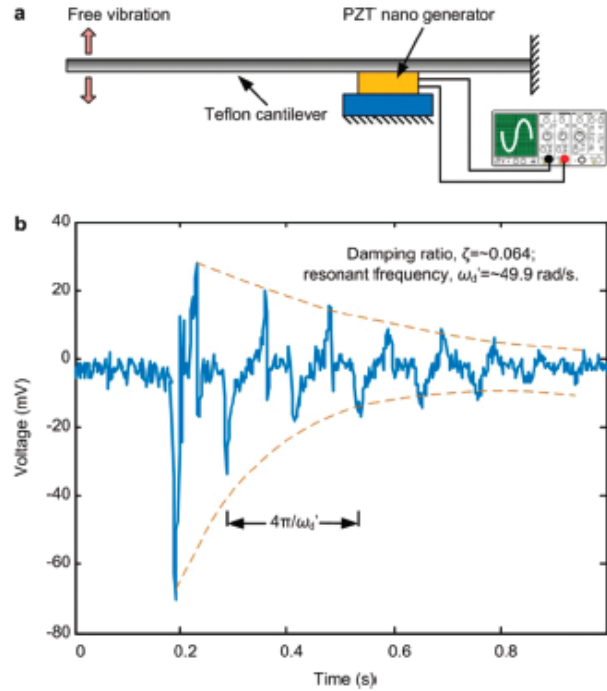


Figure 4.4-3, energy harvested from the free vibration of a Teflon cantilever. (a) Schematic of the experimental setup. (b) The open circuit voltage output when the cantilever was under free vibration. Chen et al.<sup>75</sup>

Other materials such as thin films of P(VDF-TeFE) piezoelectric polymer can be fabricated as a membrane suitable for micro-generator. Jeong et al.<sup>97</sup> discuss applying a P(VDF-TeFE) piezoelectric polymer in a micro-generator as a membrane, the polymer is being deposited on a substrate by spin-coating. In this process, some changes of the mechanical properties and quality of the film are caused by the solvent which was used to dissolve the polymer. Since a solvent affects the film properties and surface stability, the thermal process was carried out at a temperature higher than melting point, which causes some falling-off in the electrical properties.

## 5. Magnetic Energy Harvesting

### 5.1 Overview

There are reports on metal-based materials that have significant phase transformation associate with mechanical force and displacement.<sup>98-99</sup> Magnetic energy harvesting often involves multimodal systems for simultaneous energy harvesting from stray magnetic and mechanical energies by combining magnetoelectric and piezoelectric effects. Such systems usually consist of a cantilever beam with tip mass and a magnetoelectric laminate attached in the center of the beam.<sup>100</sup>

## 5.2 Magnetic/Mechanical Devices

Dong et al.<sup>100</sup> investigated a multimodal system for simultaneous energy harvesting from stray magnetic and mechanical energies by combining magnetoelectric and piezoelectric effects. The system consists of a cantilever beam with tip mass and a magnetoelectric laminate attached in the center of the beam. An equivalent circuit model was proposed that predicts a summation effect for both mechanical and magnetic energies. The schematic design of the fabricated energy harvester is illustrated Figure 5.2-1a and a picture of prototype is shown in 5.2-1 b. In this magnetoelectric / laminate configuration, two PZT fiber layers with push-pull-type symmetric polarization units<sup>101</sup> were laminated together with four magnetostrictive FeBSiC ribbons. This multimodal system that can be used for harvesting mechanical vibration and magnetic energies simultaneously and the generated electric energy is the combined effect of magnetoelastoelectric and piezoelectric contributions.

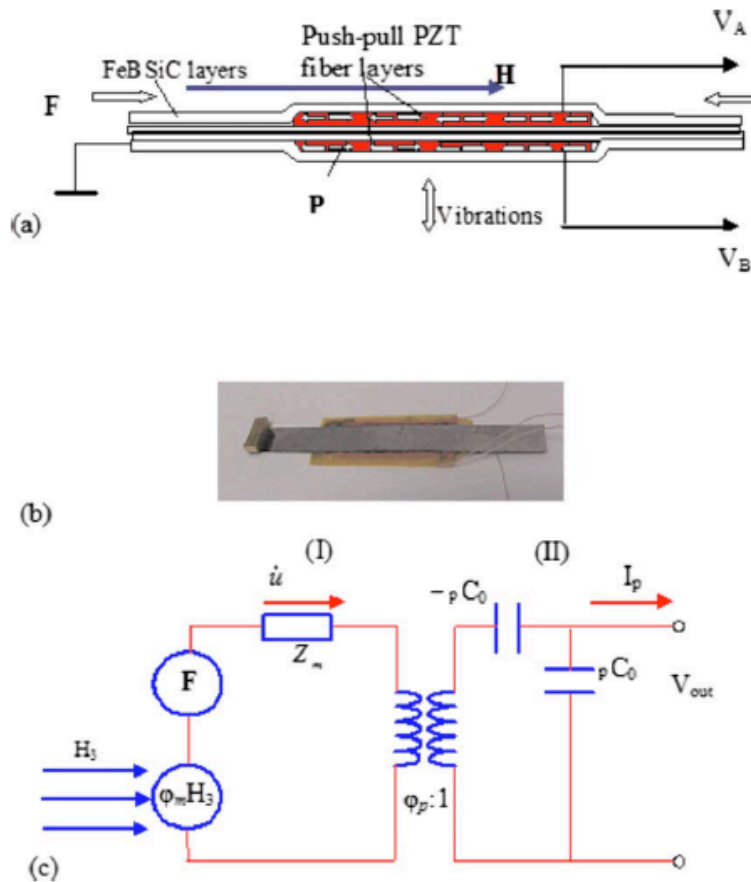


Figure 5.2-1, Conceptual illustration of the ME energy harvester: (a) schematic of the ME laminate configuration with  $p$  polarization units; (b) photo of the ME laminate prototype, and (c) equivalent circuit model for a bimechanism of EH. Dong et al.<sup>100</sup>

Wang and Yuan<sup>71</sup> report a vibration energy harvester that had two units: a device consisting a giant magnetostrictive material (MsM, Metglas 2605SC) bonded on a copper substrate

with a pick-up coil, as illustrated in Figure 5.2-2(a) along with an energy harvesting circuit. A few MsM ribbons were laminated together (Figure 5.2-2(b)). This system utilizes the effect of magnetostriction, i.e., a vibration-induced strain caused by bending producing a change in the magnetization of the laminate. While under cyclic loading, such a change is transferred into electrical energy through the coil. To enhance the energy conversion efficiency and alleviate the need of a bias magnetic field, Metglas ribbons are transversely annealed by a strong magnetic field along their width direction. The energy harvesting circuit interfaces with a wireless sensor and accumulates the harvested energy into an ultracapacitor.

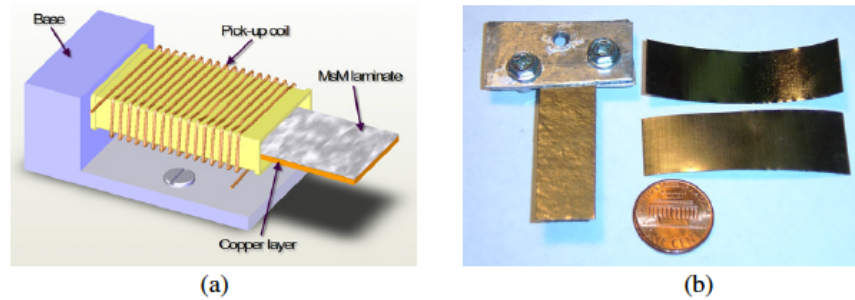


Figure 5.2-2. (a) Prototype of the MsM energy harvesting device, (b), MsM layer and laminate. Wang and Yuan.<sup>71</sup>

A rotation energy harvester employing cantilever beam and magnetostrictive/piezoelectric laminate transducer has been discussed by Li et al.<sup>70</sup> The harvester has a magnetic circuit attached to the free end of the beam, and the ME transducer is placed in the air gap of the magnetic circuit. When the harvester is attached to a host structure rotating around a horizon axis, the alternation of the gravity component causes the beam to vibrate along its transverse direction. The vibration induces an alternating magnetic field applied on the transducer, which causes the ME transducer to generate electrical power. The schematic of the proposed rotation energy harvester is shown in Figure 5.2-3. The harvester is composed of a ME transducer, a cantilever beam, and a magnetic circuit. The ME transducer is a sandwich of one PZT layer bonded between two Terfenol-D layers. The piezoelectric layer is polarized in its thickness direction, and the magnetostrictive layers are magnetized along their longitudinal direction. As the magnetic circuit moves relative to the transducer, the ME transducer induces magnetic field variations, and the changing magnetic field causes the magnetostrictive layers to generate stress. The stress is then transmitted to the piezoelectric layer, which generates electrical Power.<sup>102 103</sup>

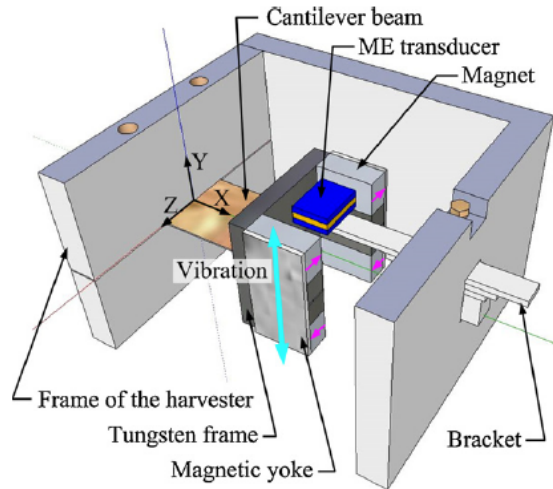


Figure 5.2-3 Schematic diagram of the proposed rotation energy harvester. Li et al.<sup>70</sup>

### 5.3 Magnetic materials

Advances in the use of magnetic materials for energy harvesting are tied to materials development. One particularly interesting route in making a wide range of magnetic materials with tailored size distributions down to the few nanometer range is spark erosion. It is possible to produce hollow particles using this technique. Spark erosion consists of generating spark discharges between electrodes immersed in a dielectric fluid. After a complex plasma creation and breakdown, molten and evaporated material is ejected from the electrodes and quenched in the dielectric.<sup>104</sup> This material condenses as particles in the dielectric liquid. The most common application of this process is electric discharge machining (EDM), used to machine hard or brittle materials. However, spark erosion is also a powerful and versatile technique to produce particles of any nominally conductive material.<sup>105 106</sup> It has been used to produce particles of metals, alloys, and compounds of a wide range of materials with particle sizes down to several nanometers.<sup>107 108</sup> Figure 5.3-1 shows examples of interesting particles produced by spark erosion. Hollow spherical particles of Ni, CoFe, the ferromagnetic shape memory alloy  $\text{Ni}_{49}\text{Mn}_{30}\text{Ga}_{21}$ , and the giant magnetostrictive alloy  $\text{Fe}_{83}\text{Ga}_{17}$ , with diameters up to several tens of microns were produced by spark erosion, using liquid nitrogen as the dielectric liquid. In contrast, the particles were primarily solid when the dielectric liquid was argon. The wall thickness of the hollow particles depends on the elemental composition.<sup>107</sup>

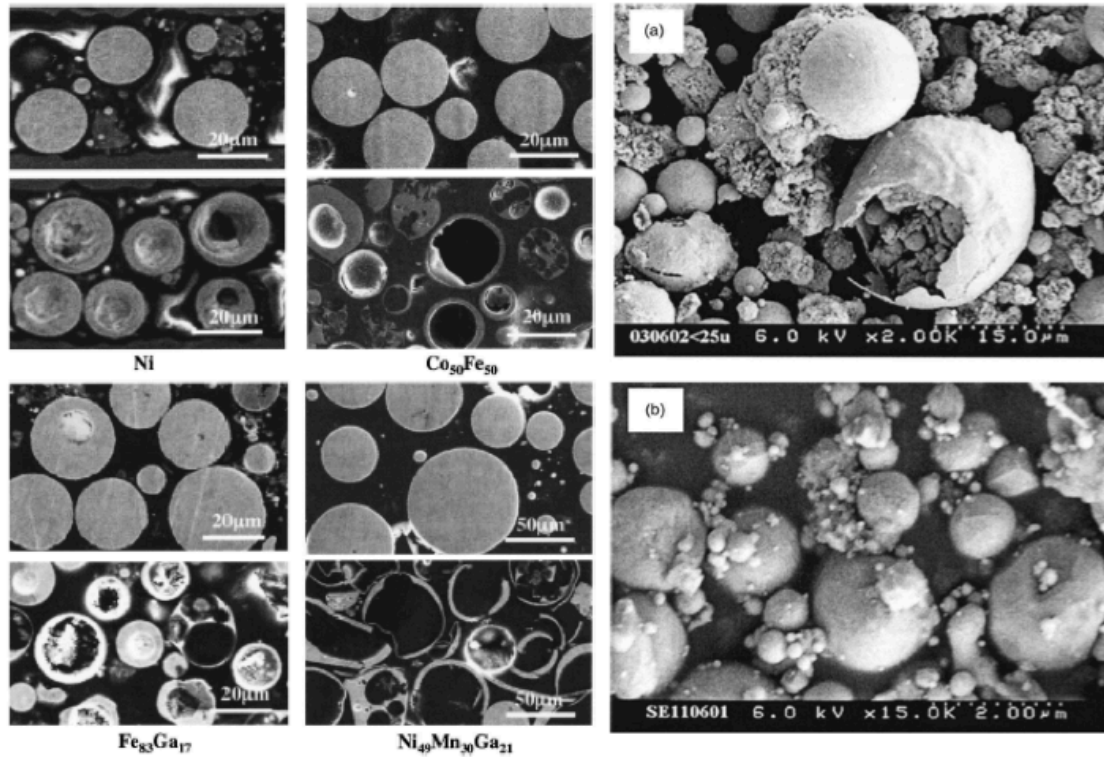


Figure 5.3-1 Examples of hollow and solid spark eroded particles. Left side: SEM micrographs of mechanically polished cross sections of as prepared particles of Ni,  $\text{Co}_{50}\text{Fe}_{50}$ ,  $\text{Fe}_{83}\text{Ga}_{17}$ , and  $\text{Ni}_{49}\text{Mn}_{30}\text{Ga}_{21}$  spark eroded in liquid argon (upper) and liquid nitrogen (lower). **Error! Bookmark not defined.** Right side: SEM micrographs of hollow and solid Ni particles. <sup>109</sup>

## 6. Combined Energy Harvesting Techniques

### 6.1 Overview

The combination of a couple or more types of energy transfer is becoming increasingly important. Combinations involving magnetostrictive materials were discussed above in Section 5. Table 1 is comparison of combination energy harvesting techniques from Wang and Yuan.<sup>71</sup>

**Table 1.** Summary of the comparison of the different vibrational types of harvesting mechanisms.

| Type             | Advantages   | Disadvantages   |
|------------------|--|---|
| Electromagnetic  | <ul style="list-style-type: none"> <li>- no need of smart material</li> <li>- no external voltage source</li> </ul>  | <ul style="list-style-type: none"> <li>- bulky size: magnets and pick-up coil</li> <li>- difficult to integrate with MEMS</li> <li>- max. voltage of 0.1 V</li> </ul>   |
| Electrostatic    | <ul style="list-style-type: none"> <li>- no need of smart material</li> <li>- compatible with MEMS</li> <li>- voltages of 2–10 V</li> </ul>  | <ul style="list-style-type: none"> <li>- external voltage (or charge) source</li> <li>- mechanical constraints needed</li> <li>- capacitive</li> </ul>  |
| Piezoelectric    | <ul style="list-style-type: none"> <li>- no external voltage source</li> <li>- high voltages of 2–10 V</li> <li>- compact configuration</li> <li>- compatible with MEMS</li> <li>- high coupling in single crystals</li> </ul> | <ul style="list-style-type: none"> <li>- depolarization</li> <li>- brittleness in bulk piezolayer</li> <li>- poor coupling in piezo-film (PVDF)</li> <li>- charge leakage</li> <li>- high output impedance</li> </ul> |
| Magnetostrictive | <ul style="list-style-type: none"> <li>- ultra-high coupling coefficient <math>&gt;0.9</math></li> <li>- no depolarization problem</li> <li>- high flexibility</li> <li>- suited to high frequency vibration</li> </ul>        | <ul style="list-style-type: none"> <li>- nonlinear effect</li> <li>- pick-up coil</li> <li>- may need bias magnets</li> <li>- difficult to integrate with MEMS</li> </ul>   |

## 6.2 Nanodevices

Wang et al.<sup>45</sup> have demonstrated an organic/inorganic hybrid energy-harvesting platform, based on nanostructured piezoelectric arrays embedded in an environmental-responsive polymer matrix, which can self-generate electrical power by scavenging energy from the environment. The device layout takes advantage of the collective stretching motion of piezoelectric ZnO NWs, induced by the shape change of the matrix polymer, to convert the thermal energy into direct current with output power densities of 20 nW/cm<sup>2</sup> at a heating temperature of 65 °C. The device relies on the response of a polymeric film to drive the piezoelectric induced by external forces, but rather caused by the shape change in the polymer matrix as it responds to external stimuli. With this hybrid approach, the NWs are near uniformly distributed inside the polymer matrix and can deform collectively under stimulation, thus each individual piezoelectric transducer can contribute power to the device. A schematic of the nanoconverter (NC) is shown in Figure 6.2-1a. The scanning electron microscopy (SEM) image of the as-grown ZnO NWs (Figure 1b) shows the nanowire diameters ranging from 60-120 nm, lengths between 7-10  $\mu\text{m}$ , and an areal density of 30/ $\mu\text{m}^2$ . A typical SEM image of the exposed NW tips (0.5  $\mu\text{m}$  long) is shown in Figure 6.2-1c. Figure 6.2-1d displays a characteristic I-V curve of a fabricated NC array that shows the current rectification behavior of the device and a turn on voltage of  $\sim 400$  mV.

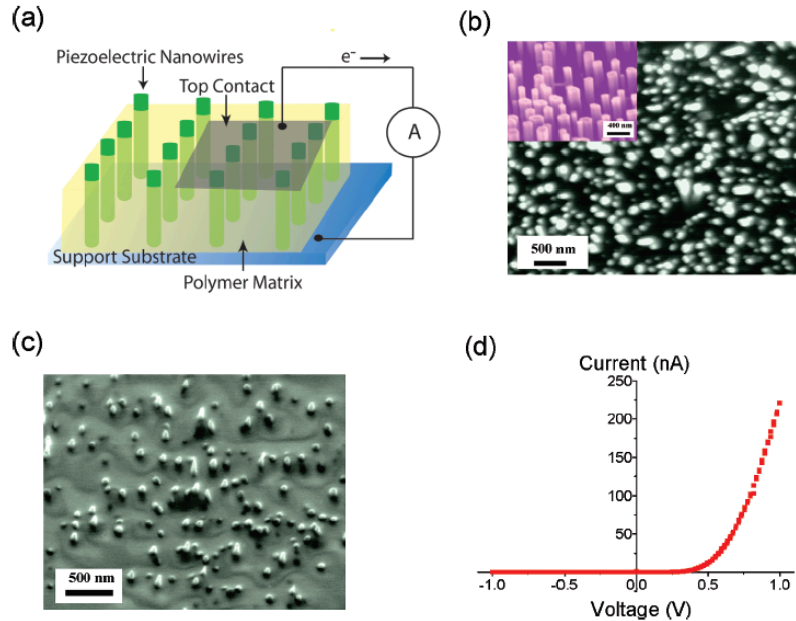


Figure 6.2-1 Design and fabrication of a ZnO-PVC polymer hybrid energy nanoconverter (NC). (a) schematic of an NC device. (b) top-view SEM image of the as-grown ZnO NWs on sapphire. The density of the NWs is about  $30 \mu\text{m}^2$ . Inset: 300° tilt view of the vertically aligned ZnO NWs. (c) A SEM image of the nanowire array after infiltrating with the PVD polymer and oxygen plasma etching. About 50 % of the NWs are exposed after plasma etching. (d) A characteristic I-V plot of an NC device showing rectification behavior and a turn-on voltage of  $\sim 400 \text{ mV}$ . Wang et al.<sup>45</sup>

To get a better understanding of the thermal gradient across the polymer film, Wang et al.<sup>45</sup> measured the temperature at the top of the polymer surface and the top of the ZnO thin film, as shown in Figure 6.2-2. To differentiate the thermoelectric from the piezoelectric potential, the device was to about  $42^\circ\text{C}$ . As illustrated in Figure 4b, the isothermally heated NC device produced an output potential that was about  $0.4 \text{ mV}$  less than the potential produced with a similar device heated from the backside only (Figure 2c). Comparing the output performance of the isothermally and bottom-heated devices suggests that over 94% of the electric potential generated comes from the piezoelectric contributions.<sup>110</sup>



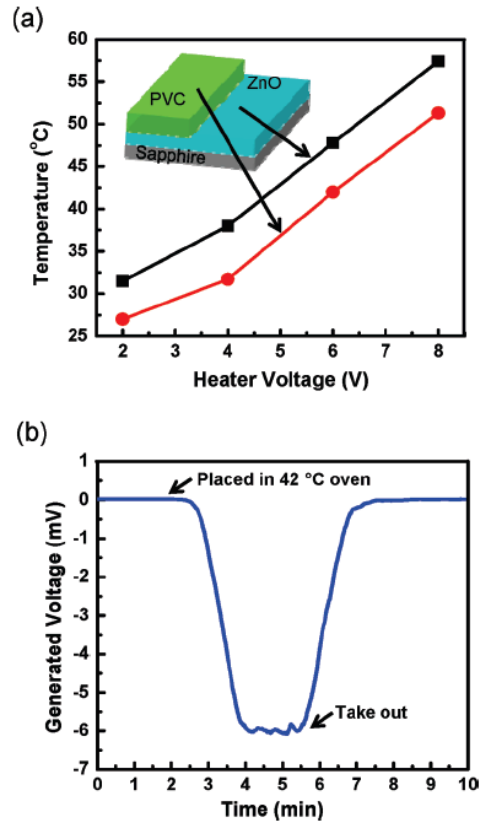


Figure 6.2-2 Thermoelectric contribution in an NC device. (a) Temperatures measured at the top and bottom of the polymer. The temperature was recorded after heating the device for 1 min. the estimated heating rate of the device is 0.23 °C/s. (b) The voltage generated from an isotropically heated 42 °C NC device. The maximum voltage is ~0.4 mV lower than a device heated from the bottom.<sup>45</sup>

### 6.3 Vibration Energy Transfer

Mechanical vibration energy which can be harvested with resonant mechanical structures excited by the vibrations is discussed by Jean-Mistral et al.<sup>66</sup>. This scavenged energy is then transformed into electricity by piezoelectric materials. They used thin piezoelectric layers deposited on the resonant structure. Dielectric polymers are passive materials. The electrical energy produced during a cycle is basically a variation of the energy stored inside a deformable capacity. An energy cycle is composed of four phases: stretch, charge, active phase and discharge. The polymer is stretched (phase A to B) then polarized (phase B to C) thus storing a given input energy (point C). To increase this stored energy, the capacity of the structure is altered by mechanical deformation (phase C to D): this is the active phase. For instance, for a cycle at constant charge  $Q$  the capacity decreases while the voltage rises ( $Q = CV$ ) thus increasing the stored energy. Finally, all charges are removed from the structure and the material can return to its initial dimensions (phase D to A). The final electrical energy is the input energy, augmented by the electrical energy effectively produced by the process described. Figure 6.3-1 shows that through configuration of dielectric polymers, an energy cycle can be established.



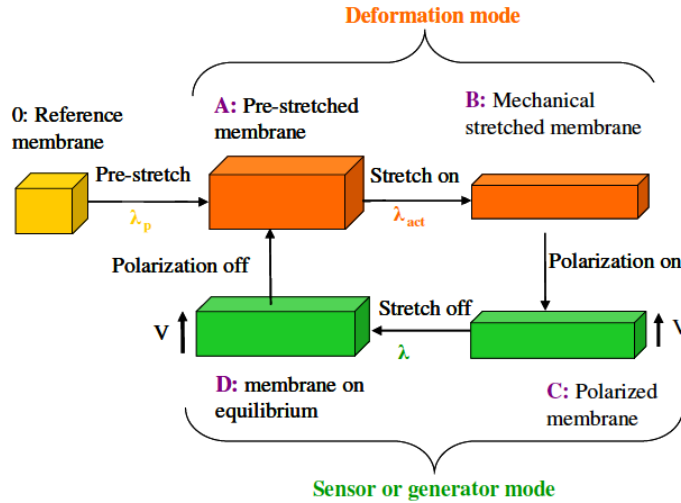


Figure 6.3-1, energy cycle for a dielectric polymer. Jean-Mistral et al.<sup>66</sup>

Jean-Mistral et al.<sup>66</sup> discuss an example as shown in Figure 6.3-2 where the VHB 4910 polymer can be used for energy conversion. This structure scavenges 0.1 mJ at 260 V for a cycle at constant voltage  $V$ , and 0.1 mJ at 170 V for a cycle at constant charge  $Q$ .

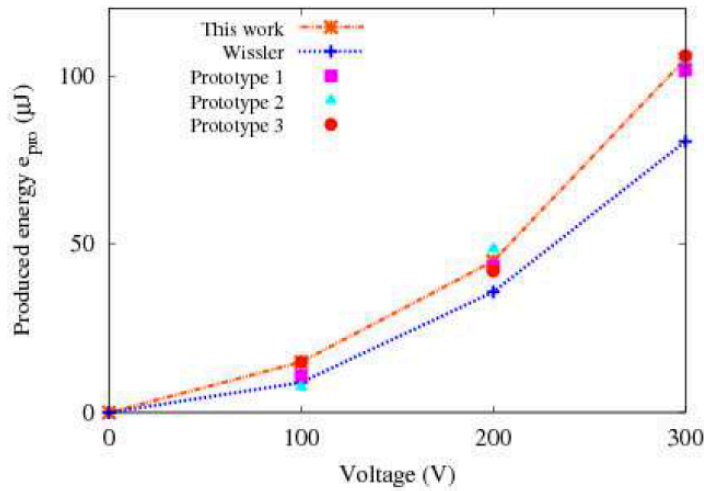


Figure 6.3-2, Energy scavenger using VHB 4910 polymer from 3M. Jean-Mistral et al.<sup>66</sup>

Cantilevers in multilayer thin film architectures have been reported by Vasta et al.<sup>94</sup>. Figure 6.3-3 shows an example of the device made of lead-free piezoelectric materials. The three architectures are:  $\text{SrRuO}_3/\text{BaTiO}_3/\text{MgO}/\text{SrTiO}_3/\text{YBa}_2\text{Cu}_3\text{O}_7$ ,  $\text{SrRuO}_3/\text{BaTiO}_3/\text{SrRuO}_3/\text{YBa}_2\text{Cu}_3\text{O}_7$  and  $\text{SrRuO}_3/\text{BaTiO}_3/\text{SrRuO}_3/\text{SrTiO}_3/\text{YBa}_2\text{Cu}_3\text{O}_7$ . It is shown that the different architectures allow a choice of the orientation of the polar axis in piezoelectric layers, in plane ( $d_{33}$  mode) or out of plane ( $d_{31}$  mode). The residual stress after the release of the cantilevers produces an upward bending, the distance between the cantilever tips and the substrate varies between 20  $\mu\text{m}$  and 45  $\mu\text{m}$ . This distance would allow the sufficient vibration amplitude to enable the cantilevers to be used as micro-generators.

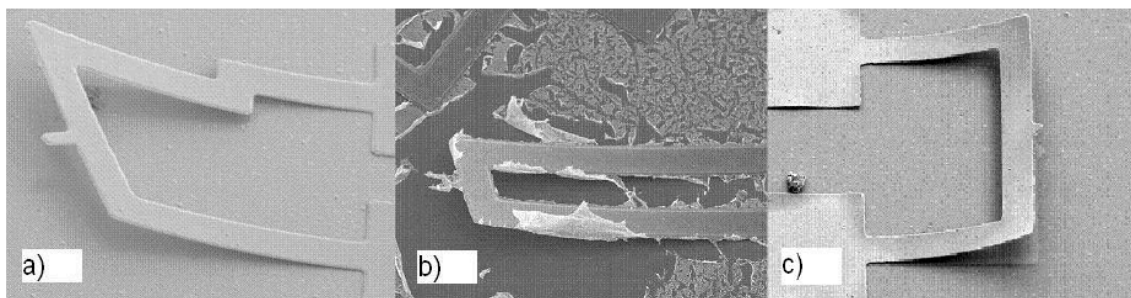


Figure 6.3-3, (a)  $\text{BaTiO}_3$  (120nm)/ $\text{MgO}$ (50nm)/  $\text{SrRuO}_3$  (500nm), 170  $\mu\text{m}$  long u-shape cantilever grown on 400 nm  $\text{YBa}_2\text{Cu}_3\text{O}_7$ . (b)  $\text{BaTiO}_3$  (120nm)/ $\text{SrTiO}_3$ (500nm), 300  $\mu\text{m}$  long u-shape cantilever grown on 400 nm  $\text{YBa}_2\text{Cu}_3\text{O}_7$ . The  $\text{YBa}_2\text{Cu}_3\text{O}_7$  layer in this case was removed by wet etching, rather than ion-beam milling, which has produced a much less well defined cantilever compared with ion milling. (c),  $\text{SrRuO}_3$ (50nm)/  $\text{BaTiO}_3$ (100nm)/ $\text{SrRuO}_3$ (350nm) 128  $\mu\text{m}$  long u-shape cantilever grown on 400 nm  $\text{YBa}_2\text{Cu}_3\text{O}_7$ . Vasta et al.<sup>94</sup>

## 6.4 Solar Thermoelectric

Recent advances in solar thermoelectric power generation are discussed by Deng and Liu.<sup>111</sup> They pointed out that direct solar thermal power generation technologies, such as thermoelectric, thermionic, magneto- hydrodynamic, and alkali-metal thermoelectric methods, are attractive methods to provide electric energy from solar heat. Figure 6.4-1 shows a schematic of one possible configuration. Muto and Chen report using a solar thermoelectric topping cycle to increase the overall efficiency. This analysis is a one-dimensional, steady state model of the heat and work transfer, and is discussed further in Section 7.4d. Parabolic trough concentrators have been found to be economical and reliable but their efficiency is limited by the maximum temperature of the heated fluid. The solar thermal trough collector is not a good application for a  $ZT=1$  thermoelectric material. To increase the overall power output of the system by approximately 10% would require a  $ZT=3$  material.<sup>57</sup>

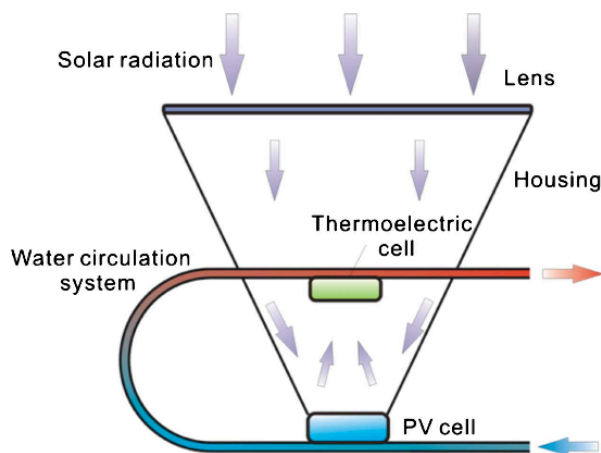


Figure 6.4-1 Separated structure combining PV and thermoelectric conversion. Deng and Liu<sup>111</sup>, originally from Hecht.<sup>112</sup>

## 7. Modeling of Energy-Harvesting Devices and Materials

### 7.1 Overview

Various models have been developed to predict maximum energy. A study on a dielectric elastomer generator (DEG) reported that the maximum amount of energy to be harvested was constrained by various modes of failure and operational limits.<sup>113</sup> Known limiting mechanisms include electrical breakdown, electromechanical instability, loss of tension and rupture by stretch. These limits define a cycle where maximum energy can be harvested. The cycle was represented on work-conjugate planes, which can be used as a guide for the design of practical cycles. The amount of energy harvested is larger when a DEG is subject to equal-biaxial stretching. In this section we discuss not only the modeling of energy harvesting devices, but the properties of the materials involved as well.

### 7.2 Band Structure

Density Functional Theory (DFT) has been used to study electronic properties in energy harvesting materials. Aguilera et al.<sup>58</sup> discuss intermediate-band material based on thiospinel semiconductor  $\text{MgIn}_2\text{S}_4$ . This material is proposed as high efficiency photovoltaic material for intermediate-band solar cells. Figure 7.2-1 compares the charge density of spin-up and spin-down. This figure shows that the spin polarization appears around the inserted transition metal.<sup>58</sup>

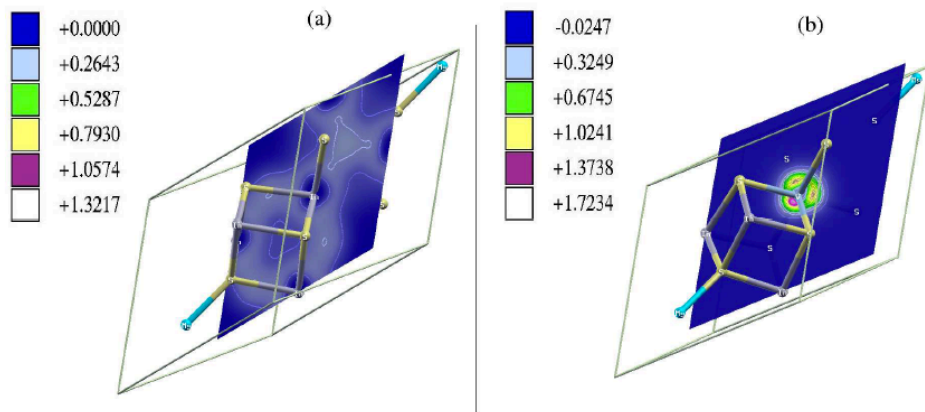


Figure 7.2-1, Electronic-charge density of (a)  $\text{MgIn}_2\text{S}_4$  and (b) difference between spin-up and spin-down density for the V-substituted alloy. Aguilera et al.<sup>58</sup>

### 7.3 Modeling Charge Transfer

Ionic thermoelectric phenomenons have been simulated based on the consideration of Grotthuss, hopping mechanism for the proton conductivity.<sup>33</sup> The Grotthuss mechanism is the protonhopping-mechanism where each oxygen atom simultaneously passes and receives a single hydrogen atom. Due to interaction with the wall of a pore, localized water molecules create deeper traps for protons than those in the bulk water. Figure 7.3-1 illustrates the mechanism of ionic diffusion.<sup>114</sup>

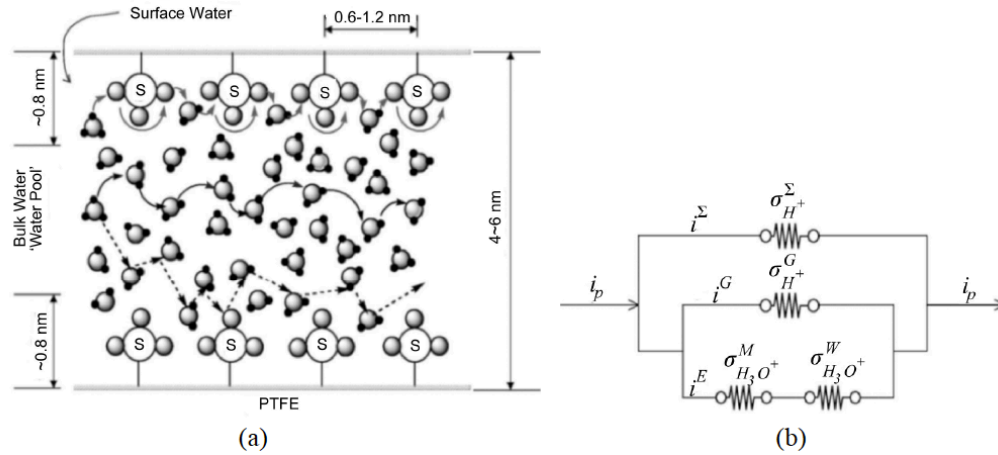


Figure 7.3-1, A simplified picture of structure and proton transfer in Nafion (a) in fully hydrated state, and (b) electrical analog of the proton transport in Nafion. Reznikov<sup>33</sup>, originally from Choi et al.<sup>114</sup>

## 7.4 Modeling Thermoelectric Properties

### 7.4a Modeling Thermoelectric Efficiency

Yazawa and Shakuri<sup>36</sup> have developed generic model of a thermoelectric power generation system which is based on cooptimizing the thermoelectric module together with the heat sink. Using this model, efficiency at maximum output power is calculated and is shown to approaches the Curzon-Ahlborn (also know as the Chambadal-Novikov-Curzon-Ahlborn) efficiency limit at very large  $Z$  values. Approaching this limit is consistent for thermodynamic systems with irreversible heat engines, and is a lower limit than found for a Carnot cycle in a reversible heat engine. Figure 7.3-2 shows the efficiency at the max at high  $ZT$ s.

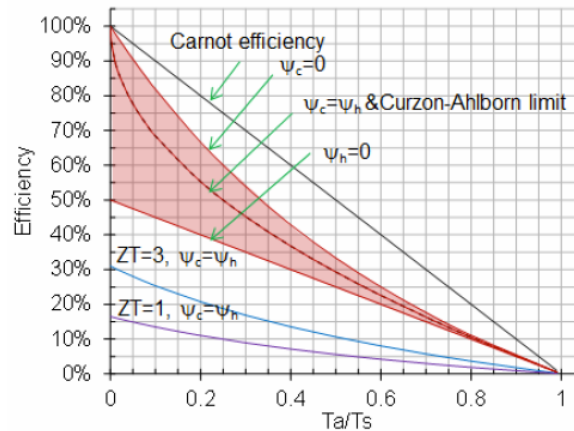


Figure 7.4a-1 Efficiency at maximum output power as  $Z$  approaches infinity, for symmetric and asymmetric thermal resistance. Curves for  $ZT=1$  and 3 are shown as well. Yazawa and Shakuri<sup>36</sup>

Fig. 7.4a-2 shows the normalized power output and heat flux from the hot reservoir as a function of the thermal resistance ratio. The maximum output is reached when the system is

symmetric at high ZT's. The maximum output is found when the system is symmetric at very high ZT's. In practice when  $ZT < 5$ , the maximum output power is obtained when the cold side thermal resistance is much smaller than the hot side. This has implications on the design of energy harvesting systems since it implies a compromise between the heat sink and optimizing the thermoelectric module.<sup>36</sup>

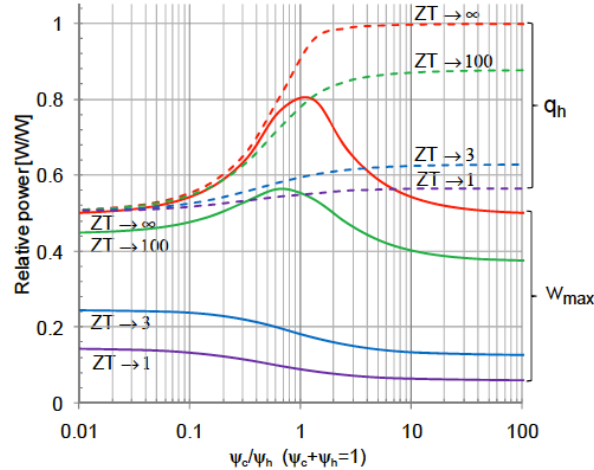


Figure 7.4a-2, Relative power output heat flow as a function of the thermal resistance ratio for different ZT values. Yazawa and Shakuri<sup>36</sup>

#### 7.4b Modeling Thermoelectric Generators

Freunek et al.<sup>115</sup> describe an analytical physical model for thermoelectric generators (TEGs). The model includes the Thomson effect, the Peltier heat, a parameterization of the Joule heat, as well as all thermal and electrical resistances. Figure 7.4b-1 shows basic physical effects taking place in a TEG. Figure 7.4b-2 demonstrates the necessity of taking into account the Peltier effect for the output power.

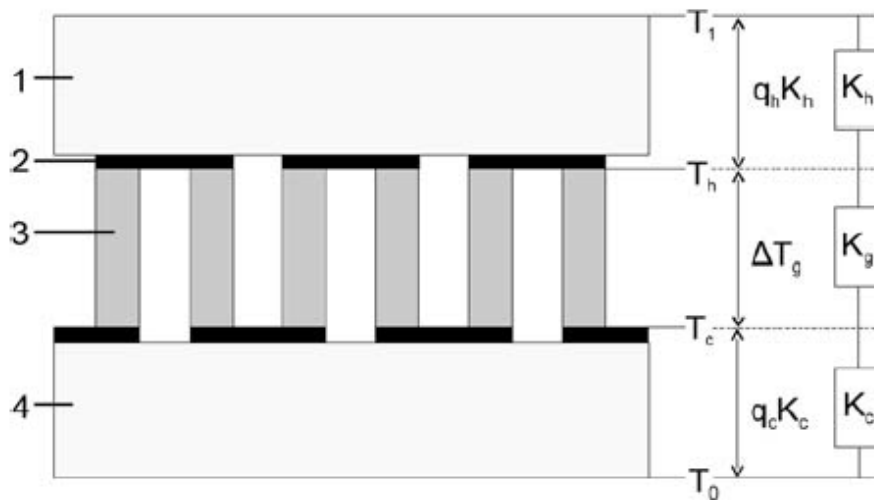


Figure 7.4b-1, Thermoelectric generator. 1, thermal resistance of wafer and the contact to the heat source; 2, conducting strip; 3, thermo legs; 4, thermal resistance of wafer and cooler; and the contact to the heat sink. Freunek et al.<sup>115</sup>

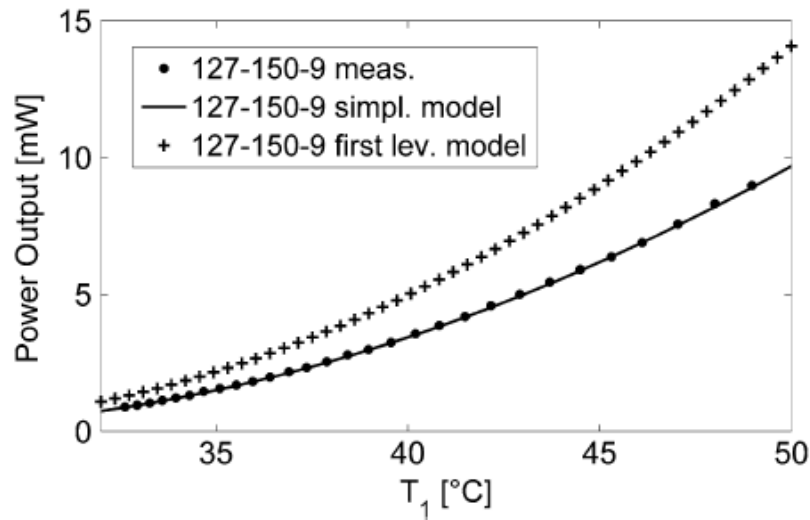


Figure 7.4b-2, comparison of the simplified model with the first-level model, revealing the influence of the Peltier effect on the output power. Freunek et al.<sup>115</sup>

#### 7.4c Modeling ZT

A number of groups have calculated the thermoelectric figure of merit using the first-principles density-functional theory.<sup>116 117 118</sup> Demchenko et al.<sup>117</sup> discuss using a nearly parameter-free theory of the thermoelectric properties of semiconductor nanowires, combining molecular dynamics, density functional theory, and Boltzmann transport theory methods to provide a complete picture for the competing factors of thermoelectric figure of merit. For ZnO and Si nanowires the figure of merit can be increased as much as 30 times in 8-Å-diameter ZnO nanowires and 20 times in 12-Å-diameter Si nanowires, compared with the bulk as shown in Figure 7.4c-1.

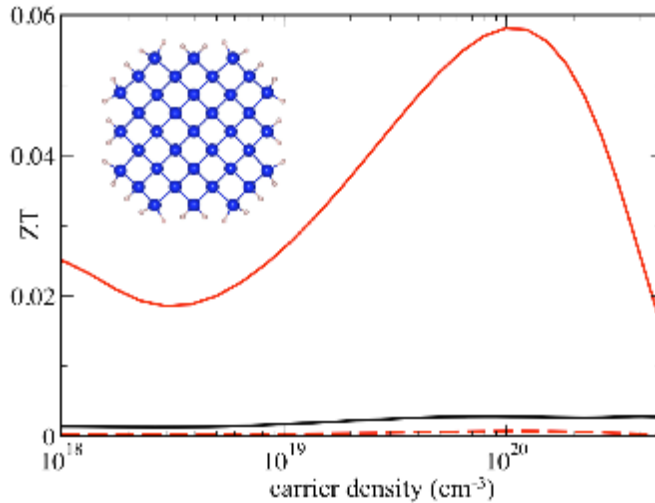


Figure 7.4c-1 ZT of 12 angstrom-diameter Si NW's (red) and bulk Si (black). The dashed (red) line is the ZT of the same Si NW calculated with bulk lattice thermal conductivity. The inset shows the cross-section atomic configuration of the NW. The NW axis direction is [001]. The lattice contributions of thermal conductivity of bulk Si and the NW, 254 and 2.8 W/Km, respectively, were derived from MD calculations. Demchenko et al.<sup>117</sup>

#### 7.4d Modeling Solar Thermoelectric Systems

Muto and Chen<sup>57</sup> discuss the possibility of adding a thermoelectric power generator (TEG) as a topping cycle at high temperature to increase the overall efficiency of a solar thermoelectric system. The analysis considered a one-dimensional, steady state model of the heat and work transfers, as shown in Figure 7.4d-1. As discussed in Section 6.4, the solar thermal trough collector is not a good application for a  $ZT = 1$  thermoelectric material.

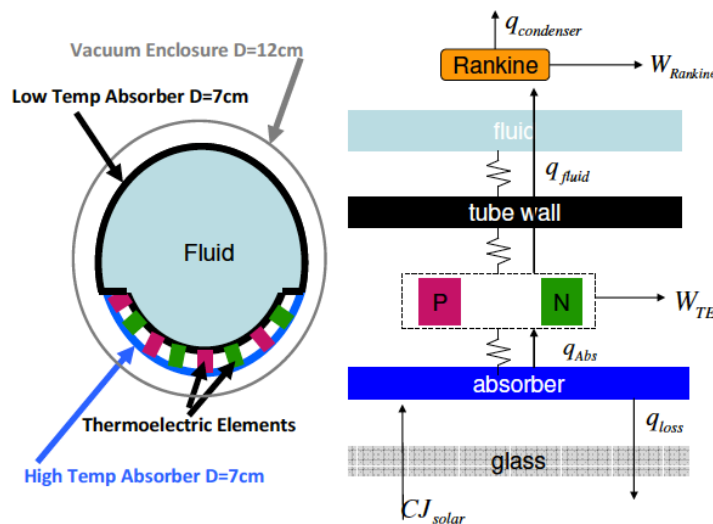


Figure 7.4d-1, Left, Schematic of the STET receiver with thermoelectric elements lining the bottom perimeter where the highest intensity concentrated radiation is located. Right: a one-dimensional steady state model of the work and heat transfers of the STET. Muto and Chen<sup>57</sup>



Oksanen and Tulkki<sup>119</sup> discuss a thermoelectric heat pump (THP) engine based on photon assisted heat transfer between two large-area light emitting diodes coupled by the electromagnetic field. The system is proposed to contain a semiconductor structure with a nearly homogeneous refractive index. The THP allows heat transfer and electricity generation at the Carnot efficiency, but there are various factors which will limit the efficiency. A numerical model to account for the most important losses of the thermophotonic heat pump shows that the thermophotonic heat pump has potential to outperform heat pumps based on the thermoelectric effect, particularly for heat transfer across large temperature differences. A schematic picture of the THP is shown in Figure 7.4d-2.

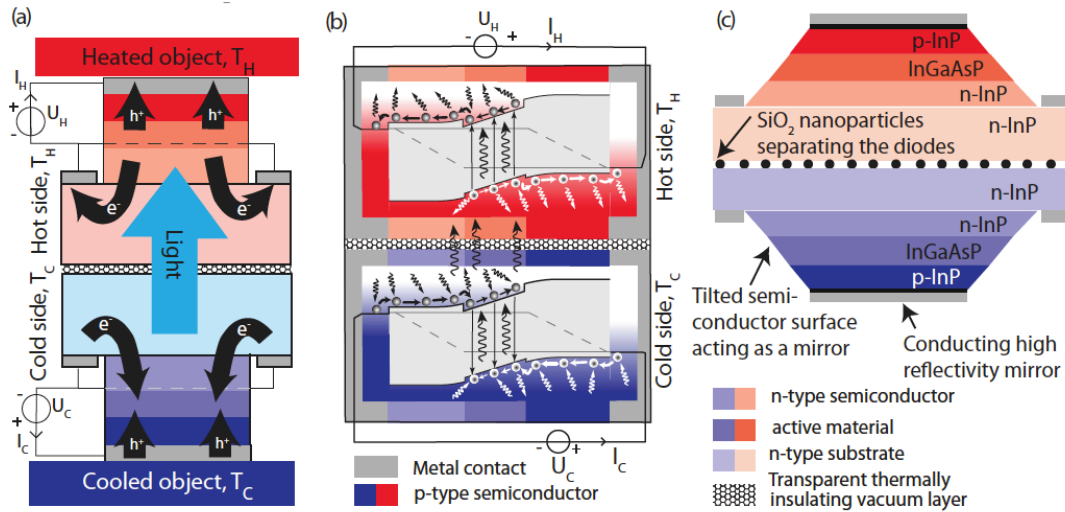


Figure 7.4d-2. A schematic diagram of the heat transfer and structure of the thermophotonic heat pumps. (a) The THP is made of two optically coupled large area (possibly a few cm<sup>2</sup>) light emitted diodes at temperatures  $T_C$  and  $T_H$  placed one on the other and separated by a thin layer of transparent thermally insulated material. (b) The energy band diagram of the thermophotonic heat pump illustrates the energy transfer in the device. Electrons (dark circles) and holes (light circles) injected by an external power supply transport electrical energy and heat energy absorbed from phonons (short curly arrows). The photons are transported to the active region of the hot side, where a part of their energy is transformed back to electrical energy. The rest is released as heat (phonons). The darker – lighter color gradient describes the electron distribution in the structure; dark color corresponds to filled electron states and light color to empty electron states. Note that the band diagrams in (b) have been rotated by 90° with respect to (a) in real space for clarity. (c) An example of a possible structure and materials for a THP. A hybrid mirror consists of a combination of Bragg mirrors and an appropriate reflective coating. To scale up the cooling power several THP structures can be integrated on the same semiconductor substrate. Oksanen and Tulkki<sup>119</sup>



## 7.5 Modeling Nanostructures

Shelly and Mostafi<sup>118</sup> discuss the thermoelectric figure of merit,  $ZT$  for p-type Si nanowires with axial Ge heterostructures using a combination of first-principles density-functional theory, interatomic potentials, and Landauer-Buttiker transport theory. Other examples were included in Section 7.4c. Example nanowire structures are shown in Figure 7.5-1. In all cases studied, a decrease of the thermoelectric power factor is observed when a heterostructure is introduced, and any increase in the figure of merit  $ZT$  is due to a corresponding reduction in lattice thermal conductivity. The dependence of these parameters on heterostructure length are shown in Figure 7.5-2.

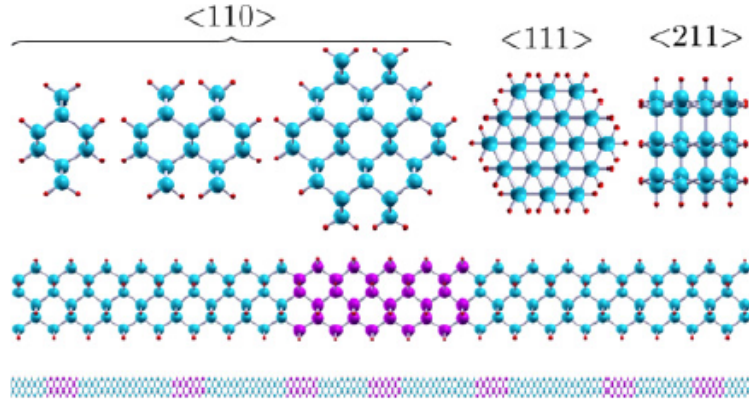


Figure 7.5-1, top: Cross-section of SiNWs. Labels indicate the crystal direction of the longitudinal ( $z$ ) axis (pointing into the page). Diameters (left-to-right): 0.78 nm, 1.02 nm, 1.44 nm, 1.14 nm, and 1.06 nm. Middle: A single Ge heterostructure in a SiNW (Ge and Si atoms in magenta and blue, respective). Bottom: A multiple heterostructure nanowire (MHNW) with an arbitrary distribution of Ge heterostructures. Shelly and Mostafi<sup>118</sup>

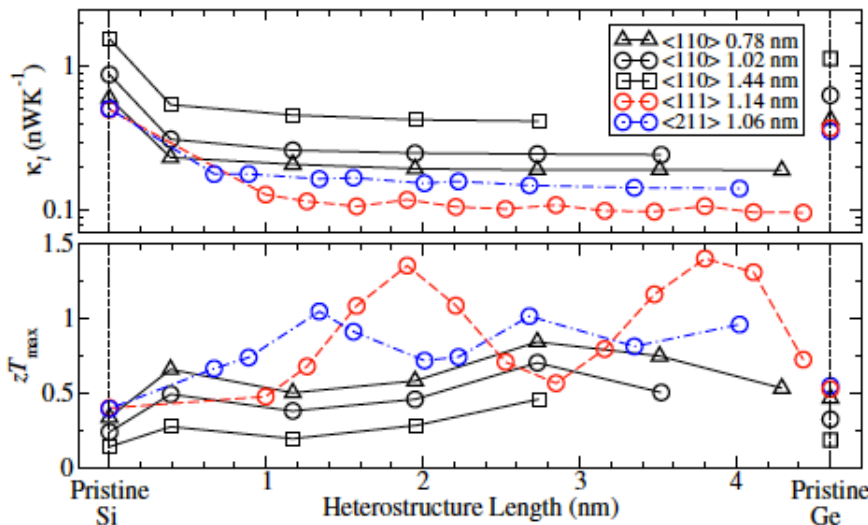


Figure 7.5-2, Dependence of  $k_1$  (top panel) and  $zT_{\max}$  (bottom) at 300 K as a function of Ge heterostructure length for  $\langle 110 \rangle$ ,  $\langle 111 \rangle$ , and  $\langle 211 \rangle$  SiNWs. Labeling is equivalent to previous figure, plotting pristine SiNWs as zero heterostructure length and pristine Ge NWs also shown on the right. Shelley and Mostofi.<sup>118</sup>

## 7.6 Modeling Mechanical Energy Harvesting

Computer simulations have been performed on energy transfer through a dielectric elastomer generator (DEG).<sup>113</sup> It was reported that the maximum energy harvested from a DEG is constrained by various failure modes and operational limits. Figure 7.6-1 shows the calculation of in-plane stress and electric field using Neo-Hookean strain energy function. Results can be used to avoid the electron breakdown, and estimate the elastic strain energy.

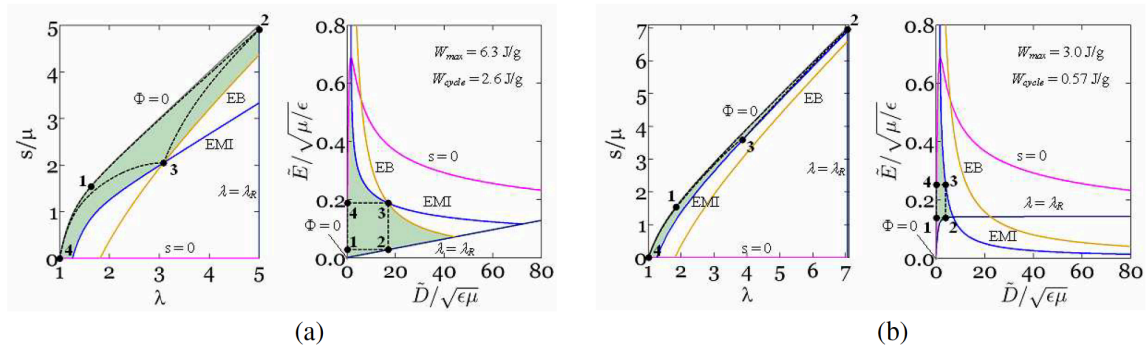
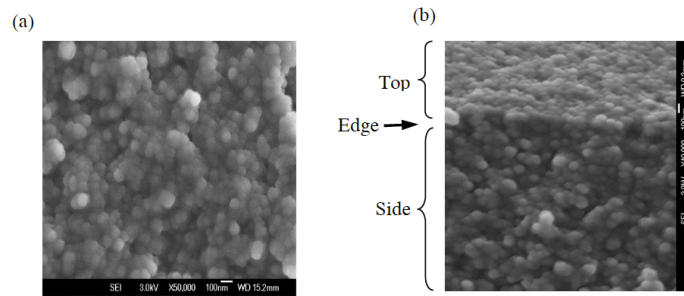


Figure 7.6-1 Electromechanical energy conversion cycles defined in planes of work-conjugate coordinates, bounded by various failure modes and operational limits for (a) Equal-biaxial stress and (b) Uniaxial stress. Koh et al.<sup>113</sup>

## 8. Nano-materials in Energy harvesting

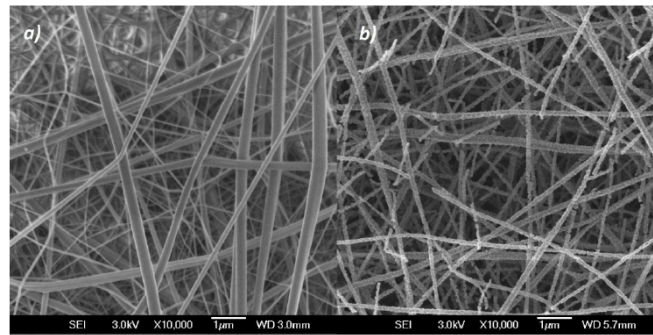
There are many reports on using nano-particles or nano-structured materials to harvest energy.<sup>21-22</sup> Throughout this review, many have been discussed previously. In this section, we will discuss specifically from a nano-materials point of view a few examples which are being used in energy harvesting research.

Carbon nanoparticles have been reported as a counter-electrode catalyst for tri-iodide reduction. The counter carbon-electrode was deposited onto fluorine-doped tin oxide (FTO) by spin coating from an aqueous colloidal suspension of the blend of carbon nanoparticles and  $\text{TiO}_2$  nanocrystals, as shown in Figure 8-1.<sup>50</sup> The carbon nanoparticle based cells have achieved an overall energy conversion efficiency of 5.55% under an illumination of 100 mW/cm<sup>2</sup>.



**Figure 8-1** a) Top view and b) cross-section SEM image of nano-crystalline TiO<sub>2</sub> films. Joshi et al.<sup>50</sup>

Hybrid piezoelectric composites have been discussed by Corral-Flores et al. as a promising material for energy harvesting.<sup>89</sup> The material was prepared by embedding barium titanate nanofibers (BTO) into a matrix of polyvinylidene fluoride (PVDF). Figure 8-2 shows the SEM image of such a material. As shown, the average diameter of fibers was in 105- 225 nm.



8-2. SEM micrographs of BTO nanofibers (a) before heat treatment and (b) sintered at 800 °C. Corral-Flores et al.<sup>89</sup>

Nanostructured thin film devices were reported for wind energy harvesting. Such device was made of piezoelectric polymers, i.e. PVDF. The device generated 1 µW power (at 15 mph wind) with a single layer of PVDF of 4 x 2" 50 µm in thickness, sandwiched between two thin gold electrode films. By adding nanotubes, the mechanical properties were further improved, as shown in Figure 8-3.<sup>93</sup>

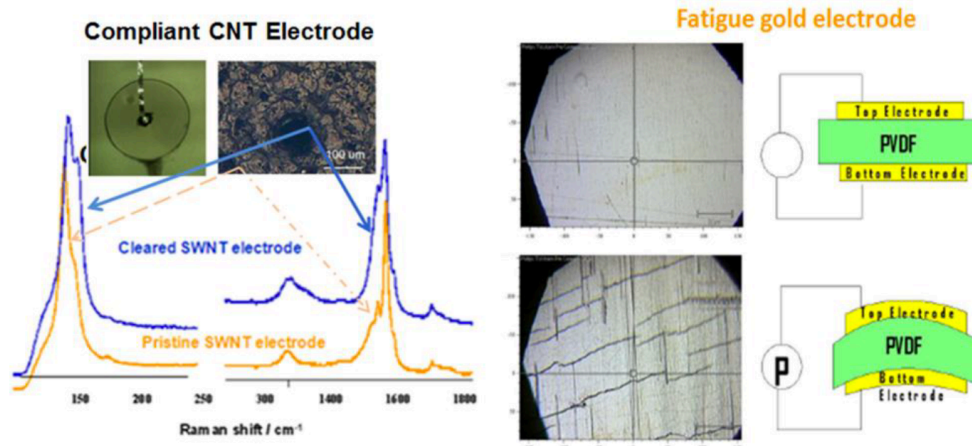


**Figure 8-3** Comparison of CNT vs. metal as electrode materials in mechanical energy conversions. On the left pane, Raman spectra show CNT in “self-clearing” areas (inset) with only electronic structure changes (not composition and structure changes), while the gold thin film electrodes on the PVDF in the right pane shows that typical metal fatigue with cracks at the micro scales. Lake et al.<sup>93</sup>

## 9. Conclusion

Energy harvesting as a discipline continues to become increasingly important for applications and ever more interesting scientifically. The goal of this review is to present an integrated view which should be of interest to a wide variety of both senior researchers and graduate students working in the field. One important aspect of energy harvesting is its sustainability from a critical materials perspective, as research success transitions into widespread practical applications. Figure 9-1 from the paper of Vaquero and Anthony Powell<sup>7</sup> makes the point that the development of high-performance thermoelectric materials should incorporate the more abundant elements such as first-row transition series elements in order to provide a long term option for wide-scale implementation of thermoelectric technology. The larger point is that this philosophy applies to all of the energy harvesting technologies that have been reviewed here.

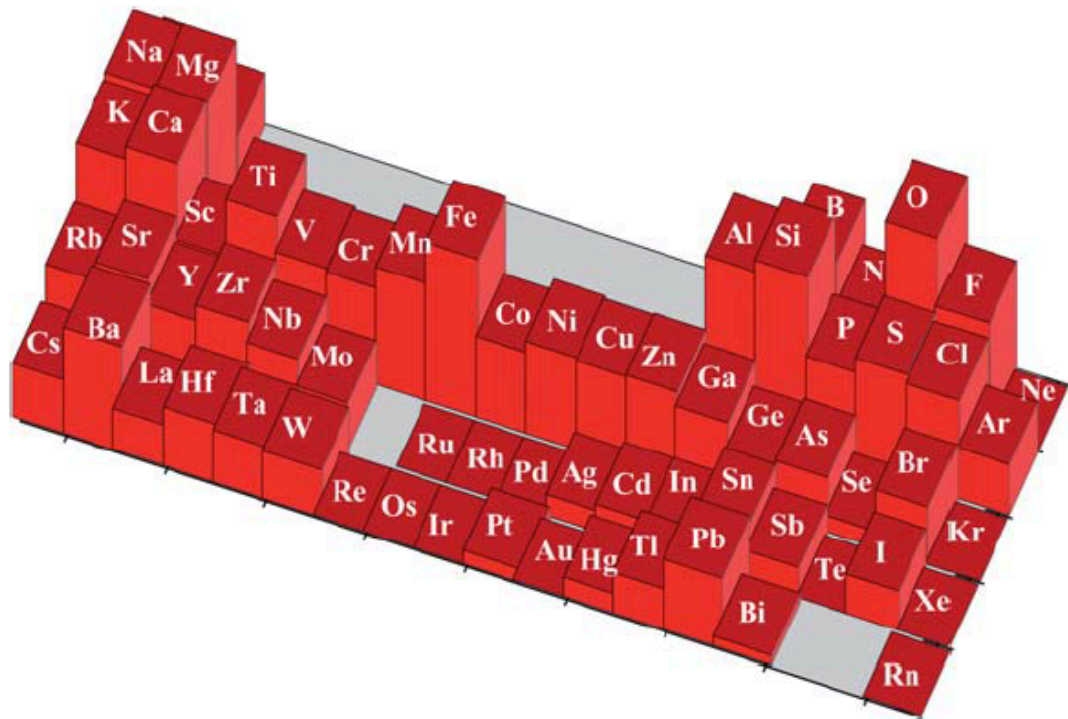


Figure 9-1. Relative abundance of the principal elements in the earth's crust, presented using a logarithmic scale. Vaqueiro and Powell.<sup>7</sup>

#### **Acknowledgments –**

This work performed under the auspices of the U.S. Department of Energy by Lawrence Livermore National Laboratory under Contract DE-AC52-07NA27344. The work at Texas A&M University is in part sponsored by the Thermal Transport Processes program at the National Science Foundation and the Texas Engineering Experimental Station.

One of the authors (HBR) wishes to thank James Holbery, Nick Kioussis, Laura Lewis, Robert O'Handley, Frank Schmidt and Rama Venkatasubramanian for helpful discussions. The other author (HL) would like to acknowledge her students and postdocs for research assistance in related areas.

## References

- <sup>1</sup> Jeannine R. Szczech, Jeremy M. Higgins And Song Jin, "Enhancement of The Thermoelectric Properties In Nanoscale And Nanostructured Materials," *J. Mater. Chem.*, 2011, 21, 4037–4055;
- <sup>2</sup> Jian He And Yufei Liu, Ryoji Funahashi, "Oxide Thermoelectrics: The Challenges, Progress, And Outlook, *J. Mater. Res.*, Vol. 26, No. 15, Aug 14, 2011.
- <sup>3</sup> Mildred Dresselhaus, "The Evolution of Nanothermoelectricity," *Mater. Res. Soc. Symp. Proc. Vol. 1329* © 2011 Materials Research Society Doi: 10.1557/Opl.2011.1233
- <sup>4</sup> D.L. Medlin A, G.J. Snyder, "Interfaces In Bulk Thermoelectric Materials: A Review For Current Opinion In Colloid And Interface Science," *Current Opinion In Colloid & Interface Science* 14 (2009) 226–235.;
- <sup>5</sup> L. D. Hicks, T. C. Harman, X. Sun, "Experimental Study Of The Effect Of Quantum-Well Structures On The Thermoelectric Figure Of Merit," *Physical Review B* Volume 53, Number 16. 1996.
- <sup>6</sup> C. Candolfi, U. Aydemir, A. Ormeci, M. Baitinger, N. Oeschler, F. Steglich, And Yu. Grin, "Low-Temperature Magnetic, Galvanomagnetic, And Thermoelectric Properties Of The Type-I Clathrates Ba<sub>8</sub>Ni<sub>13</sub>Si<sub>46</sub>–X," *Physical Review B* 83, 205102 (2011). 205102-1
- <sup>7</sup> Paz Vaqueiro And Anthony V. Powell, "Recent Developments In Nanostructured Materials For High-Performance Thermoelectrics," *J. Mater. Chem.*, 2010, 20, 9577–9584.
- <sup>8</sup> Kuei Fang Hsu, Sim Loo, Fu Guo, Wei Chen, Jeffrey S. Dyck, Ctirad Uher, Tim Hogan, E. K. Polychroniadis, Mercouri G. Kanatzidis, "Cubic Ag<sub>13</sub>Pb<sub>10</sub>Sb<sub>2</sub>Te<sub>21</sub>M: Bulk Thermoelectric Materials With High Figure Of Merit," *Science*, 6 February 2004 818-821. [Doi:10.1126/Science.1092963].
- <sup>9</sup> Brian C. Sales, "Critical Overview Of Recent Approaches To Improved Thermoelectric Materials," *Int. J. Appl. Ceram. Technol.*, 4 [4] 291–296 (2007).
- <sup>10</sup> P. Pichanusakorn And P. R. Bandaru, "Minimum Length Scales For Enhancement of The Power Factor In Thermoelectric Nanostructures," *J. Appl. Phys.* 107, 074304 (2010); 10.1063/1.3359659
- <sup>11</sup> E. Alleno, L. Chen, C. Chubilleau, B. Lenoir, O. Rouleau, M.F. Trichet, And B. Villeroy, "Thermal Conductivity Reduction In CoS<sub>3</sub>–CeO<sub>2</sub> Nanocomposites," *Journal of Electronic Materials*, Vol. 39, No. 9, 2010. Doi: 10.1007
- <sup>12</sup> Ronald F. Gibson, "A Review Of Recent Research on Mechanics Of Multifunctional Composite Materials And Structures," *Composite Structures* 92 (2010) 2793–2810.
- <sup>13</sup> K. Wang, H. Lee, R. Cooper, And H. Liang, "Time Resolved, Stress Induced, And Anisotropic Phase Transformation of A Piezoelectric Polymer," *App. Physics, A*, 95(2), 2009, Pp. 435-441.
- <sup>14</sup> H. Liang, R. Cooper, And J. Files, "Phase Transformation of Poly (Vinylidene Difluoride) In Energy Harvesting," *J. Matls. Res.*, 26 (01), Pp.1-8, 2011.
- <sup>15</sup> George S. Nolas, Joe Poon, and Mercouri Kanatzidis s, "Recent Developments In Bulk Thermoelectric Materials," *MRS Bulletin* Vol. 31 Issue: 3 Terry M.Tritt and M.A. Subramanian, Guest Editors Pages: 199-205, 2006. Doi: 10.1557/Mrs2006.45.

- 
- <sup>16</sup> P. Sahani, S. Mula, P.K. Roy, P.C. Kang, C.C. Koch, "Structural Investigation Of Vacuum Sintered Cu-Cr And Cu-Cr-4% SiC Nanocomposites Prepared By Mechanical Alloying," *Materials Science And Engineering A-Structural Materials Properties Microstructure and Processing* Volume: 528 Issue: 25-26 Pages: 7781-7789, (2011). Doi: 10.1016/J.Msea.2011.06.086 Published: Sep 25 2011
- <sup>17</sup> Jinglei Xiang and Lawrence T. Drzal., "Enhanced Thermal Conductivity Of Phase Change Materials Modified By Exfoliated Graphite Nanoplatelets," *Mater. Res. Soc. Symp. Proc.* Vol. 1218 © 2010.
- <sup>18</sup> Xun Shi, Jiong Yang, James R. Salvador, Miaofang Chi, Jung Y. Cho, Hsin Wang, Shengqiang Bai, Jihui Yang, Wenqing Zhang, And Lidong Chen, "Multiple-Filled Skutterudites: High Thermoelectric Figure Of Merit Through Separately Optimizing Electrical And Thermal Transports," *Dx.Doi.Org/10.1021/Ja111199y* | *J. Am. Chem. Soc.* 2011, 133, 7837–7846.
- <sup>19</sup> Christopher J. Vineis , Ali Shakouri , Arun Majumdar , And Mercouri G. Kanatzidis, "Nanostructured Thermoelectrics: Big Efficiency Gains From Small Features," *Adv. Mater.* 2010, 22, 3970–3980.
- <sup>20</sup> G. J. Snyder and E. S. Toberer, *Complex Thermoelectric Materials Nat. Mater.*, 2008, 7, 105–114.
- <sup>21</sup> Cham Kim, Dong Hwan Kim, Jong Sook Kim, Yoon Soo Han, Jong Shik Chung, Hoyoung Kim, "A Study of The Synthesis of Bismuth Tellurium Selenide Nanocompounds and Procedures For Improving Their Thermoelectric Performance," *Journal of Alloys And Compounds* 509 (2011) 9472– 9478.
- <sup>22</sup> Yujie Liang, Wenzhong Wang, Baoqing Zeng, Guling Zhang, Qingyu He, Junli Fu, "Influence of NaOH on The Formation And Morphology of  $\text{Bi}_2\text{Te}_3$  Nanostructures In A Solvothermal Process: From Hexagonal Nanoplates To Nanorings," *Materials Chemistry and Physics* 129 (2011) 90– 98.
- <sup>23</sup> P. N. Alboni, X. Ji, J. He, N. Gothard, And Terry M. Tritt, "Thermoelectric Properties of  $\text{La}_{0.9}\text{CoFe}_3\text{Sb}_{12}-\text{CoSb}_3$  Skutterudite Nanocomposites," *J. Appl. Phys.* 103, 113707 (2008); Doi: 10.1063/1.2937904.
- <sup>24</sup> A. Yadav, K. P. Pipe, W. Ye, And R. S. Goldman, "Thermoelectric Properties of Quantum Dot Chains," *J. Appl. Phys.* 105, 093711-17 (2009); Doi: 10.1063/1.3094029
- <sup>25</sup> Akihiro Ishida, Tomohiro Yamada, Daoshe Cao, Yoku Inoue, Martin Veis Et Al. "Seebeck Effect In PbTe Films And EuTe/Pbte Superlattices," *J. Appl. Phys.* 106, 023718 (2009); Doi: 10.1063/1.3182804
- <sup>26</sup> B. Bhushan, *Springer Handbook Of Nanotechnology*, 2<sup>nd</sup> Edition, Springer, 2007. Isbn-13: 978-3-540-29855-7.
- <sup>27</sup> J. M. Higgins, A. L. Schmitt, I. A. Guzei and S. Jin, Higher Manganese Silicide Nanowires of Nowotny Chimney Ladder Phase, *J. Am. Chem. Soc.*, 2008, 130, 16086–16094.
- <sup>28</sup> J.P. Heremans, V. Jovovic, E.S. Toberer, A. Saramat, K. Kurosaki, A. Charoenpakdee, S. Yamanaka, G.J. Snyder, Enhancement of Thermoelectric Efficiency in PbTe by Distortion of the Electronic Density of States *Science* 321 (2008) 554.
- <sup>29</sup> Sumithra Santhanam, Nathan J. Takas, Dinesh K. Misra, Pierre F.P. Poudeu and Kevin L. Stokes, "Nanocomposite Of  $\text{Bi}_2\text{Te}_3$  With Metal Inclusions for Advanced Thermoelectric Applications" *Mater. Res. Soc. Symp. Proc.* Vol. 1218, Z05-11, 2010.



- 
- <sup>30</sup> S.H. Choi, J.R. Elliott, G.C. King, And P.T. Lillehei, "Wireless Power Technology For Application-Specific Scenarios Of High Altitude Airships," Smart Structures And Materials 2006: Smart Electronics, Mems, Biomems, And Nanotechnology, Ed. By V.K. Varadan, Proc. Spie, Vol. 6172, 61721d, (2006). Doi: 10.1117/12.657 130.
- <sup>31</sup> M. S. Dresselhaus, G. Chen, M.Y. Tang, R.G. Yang, H. Lee, D.Z. Wang, Z. F. Ren, J.P. Fleurial, And P. Gogna, " New Directions For Nanoscale Thermoelectric Materials Research,' (2007), New Directions for Low-Dimensional Thermoelectric Materials. Advanced Materials, 19: 1043–1053, 2007. doi: 10.1002/adma.
- <sup>32</sup> C. Ramesh Koripella, Lon E. Bell, Doug Crane And Dazhi Wang, "Characterization Of Thermal Interface Resistance In Thermoelectric Generators," Mater. Res. Soc. Symp. Proc. Vol. 1325 © 2011 Materials Research Society, Doi: 10.1557/Opl.2011.968
- <sup>33</sup> Michael A. Reznikov, "Thermoelectric Power By The Diffusion of Protons In A Nanoporous Structure," Mater. Res. Soc. Symp. Proc. Vol. 1325 © 2011 Materials Research Society. Doi: 10.1557/Opl.2011.1116
- <sup>34</sup> S. Budak, S. Guner, T. Hill, M. Black, S. B. Judah, C. I Muntele, And D. Ila, "Fabrication And Characterization Of Thermoelectric Generators From SiGe Thin Films," Mater. Res. Soc. Symp. Proc. Vol. 1102 © 2008 Materials Research Society.
- <sup>35</sup> G. Rogl, S. Puchegger, M. Zehetbauer, A. Grytsiv, P. Rogl, "Dependence of The Elastic Moduli of Skutterudites On Density And Temperature," Mater. Res. Soc. Symp. Proc. Vol. 1325 © 2011 Materials Research Society Doi: 10.1557/Opl.2011.845
- <sup>36</sup> Kazuaki Yazawa, Ali Shakouri, "Power Generation Efficiency With Extremely Large Z Factor Thermoelectric Material," Mater. Res. Soc. Symp. Proc. Vol. 1325 © 2011 Materials Research Society Doi: 10.1557/Opl.2011.1062.
- <sup>37</sup> Terry J. Hendricks, And Naveen K. Karri, "Robust Design Of Advanced Thermoelectric Conversion Systems: Probabilistic Design Impacts on Specific Power And Power Flux Optimization," Mater. Res. Soc. Symp. Proc. Vol. 1102 © 2008 Materials Research Society.
- <sup>38</sup> Shunta Haradaa, Katsushi Tanakaa, And Haruyuki Inuia, Reduction In The Thermal Conductivity of Thermoelectric Titanium Oxide By Introduction Of Planar Defects, Mater. Res. Soc. Symp. Proc. Vol. 1218 © 2010 Materials Research Society
- <sup>39</sup> Honda, Y., Iida, T., Sakamotoa, Sakuragi, S.; Taguchi Y., Mito, Y., Nemoto, T., Nakajima, T., Taguchi, H., Nishio, H., And Takanashi, Y., "Direct Thermal-To-Electric Energy Conversion Material Consisting Of Environmentally-Benign Mg<sub>2</sub>Si Synthesized Using Waste Si Sludge And Recycled Mg Alloy," Mater. Res. Soc. Symp. Proc. Vol. 1218 © 2010 Materials Research Society 1218-Z05-17
- <sup>40</sup> Okamoto, N.L., Hashimoto, Y., Koyama, T., Adachi, H., Kishida, K., Tanaka, K., And Inui, H., "Improvement of The Thermoelectric Properties Of The Chimney–Ladder Compounds In The Ru-Mn-Si System," Mater. Res. Soc. Symp. Proc. Vol. 1218 © 2010 Materials Research Society 1218-Z06-09
- <sup>41</sup> Wu, C.I., Girard, S.N., Sootsman, J., Timm, E., Ni, J., Schmidt, R., Kanatzidis, M., Schock, H., Case, E.D., Chung, D.Y., And Hogan, T., "Thermoelectric Generators Made With Novel Lead Telluride Based Materials," Mater. Res. Soc. Symp. Proc. Vol. 1218 © 2010 Materials Research Society 1218-Z02-11.

- 
- <sup>42</sup> Takahiro Kenjo, Yoshisato Kimura And Yoshinao Mishima, "Phase Stability And Thermoelectric Properties Of Half-Heusler Compounds (Ti,M)Nis (M = Zr, Hf)," Mater. Res. Soc. Symp. Proc. Vol. 1218 © 2010 Materials Research Society 1218-Z05-14
- <sup>43</sup> W. Kim , J. Zide , A. Gossard , D. Klenov , S. Stemmer , A. Shakouri, A. Majumdar, Thermal Conductivity Reduction and Thermoelectric Figure of Merit Increase by Embedding Nanoparticles in Crystalline Semiconductors Phys. Rev. Lett. 2006 , 96 , 045901 .
- <sup>44</sup> M. Zebarjadi, K. Esfarjani, M. S. Dresselhaus, Z. F. Ren and G. Chen., "Perspectives on thermoelectrics: from fundamentals to device applications, 2006, Energy Environ. Sci., 2012, **5**, 5147 DOI: 10.1039/c1ee02497c
- <sup>45</sup> Xianying Wang, Kanguk Kim, Yinmin Wang, Michael Stadermann, Aleksandr Noy, Alex V. Hamza,† Junhe Yang, And Donald J. Sirbuly, "Matrix-Assisted Energy Conversion In Nanostructured Piezoelectric Arrays," Nano Lett. 2010, 10, 4901–4907, Doi: 10.1021/Nl102863c.
- <sup>46</sup> Paothep Pichanusakorn, Prabhakar Bandaru Materials Science And Engineering R 67 19–63, (2010)
- <sup>47</sup> R. Yang, G. Chen and M. S. Dresselhaus, Phys. Rev. B: Condens. Matter Mater. Phys., 2005, 72, 125418/1–125418/7.
- <sup>48</sup> G.D. Scholes, G.R. Fleming, A. Olaya-Castro, And R. Van Grondelle, "Lessons From Nature About Solar Light Harvesting," Nature Chemistry, Published Online: 23 September 2011 | Doi: 10.1038/Nchem.1145.
- <sup>49</sup> Mark Z. Jacobson (2009). Review Of Solutions To Global Warming, Air Pollution, And Energy Security P. 4. Energy Environ. Sci., 2009, 2, 148–173. Doi: 10.1039/B809990c.
- <sup>50</sup> Prakash Joshi, Yu Xie, Jeremiah Mwaura, Mike Ropp, David Galipeau, And Qiquan Qiao, "Carbon Nanoparticles For Counter Electrode Catalyst In Dye-Sensitized Solar Cells," Mater. Res. Soc. Symp. Proc. Vol. 1102 © 2008 Materials Research Society, 1102-LI01-05.
- <sup>51</sup> Nanditha Dissanayake, Ross A Hatton, Cristina Giusca, Thierry Lutz, Richard Curry, And Ravi Silva, "Organic:Pbs-Nanocrystal:Fullerene Hybrid Photovoltaics," Mater. Res. Soc. Symp. Proc. Vol. 1102 © 2008 Materials Research Society.
- <sup>52</sup> Chien-Tsung Wang, And Chung-Hsiao Yeh, "Quantum Dot Solar Cells Based On Cdse-Assembled Titania Semiconductors," Mater. Res. Soc. Symp. Proc. Vol. 1102 © 2008 Materials Research Society.
- <sup>53</sup> Andenet Alemu, And Alex Freundlich, "Single Carrier Resonant Tunneling Design For Improving Carrier Collection In Quantum Confined Solar Cells," Mater. Res. Soc. Symp. Proc. Vol. 1102 © 2008 Materials Research Society.
- <sup>54</sup> Vladimir Svrcek, Hiroyuki Fujiwara, And Michio Kondo, "Phosphorous And Boron Doped Colloidal Silicon Nanocrystals In Conjugated Co-Polymers," Mater. Res. Soc. Symp. Proc. Vol. 1102 © 2008 Materials Research Society.

- 
- <sup>55</sup> P.V. Kamat, "Meeting The Clean Energy Demand: Nanostructure Architectures For Solar Energy Conversion," J. Phys. Chem. C 2007, 111, 2834-2860; Kamat, P. V. Barazzouk, S. Hotchandani, S. Electrochemical Modulation of Fluorophore Emission at a Nanostructured Gold Film. Angew. Chem., Int. Ed. 2002, 41, 2764-2767; George Thomas, K.; Kamat, P. V. Chromophore Functionalized Gold Nanoparticles. Acc. Chem. Res. 2003, 36, 888-898.
- <sup>56</sup> K.J. Channon, G.L. Devlin, And C.E. Macphee, "Efficient Energy Transfer Within Self-Assembling Peptide Fibers: A Route To Light-Harvesting Nanomaterials," J. Am. Chem. Soc. 2009, 131, 12520–12521.
- <sup>57</sup> Muto, A. And Chen, G., "Thermoelectric Topping Cycle For Trough Solar Thermal Power Plant," Mater. Res. Soc. Symp. Proc. Vol. 1218 © 2010 Materials Research Society 1218-Z07
- <sup>58</sup> Aguilera, I., Palacios, P., Sánchez, L., And Wahnón, P., "Advanced Computational Design Of Intermediate-Band Photovoltaic Material V-Substituted MgIn<sub>2</sub>S<sub>4</sub>," Mater. Res. Soc. Symp. Proc. Vol. 1218 © 2010 Materials Research Society 1218-Z04-02
- <sup>59</sup> X. Zhang, M.A. Ballem, M. Ahre'N, A. Suska, P. Bergman, And K. Uvdal, "Nanoscale Ln(III)-Carboxylate Coordination Polymers (Ln ) Gd, Eu, Yb): Temperature-Controlled Guest Encapsulation And Light Harvesting," J. Am. Chem. Soc. 2010, 132, 10391–10397.
- <sup>60</sup> D.L. Andrews And D.S. Bradshaw, "Nonlinear Energy Pooling In Nanophotonic Materials," Organic Optoelectronics And Photonics, Edited By Paul L. Heremans, Michele Muccini, Hans Hofstraat, Proceedings Of Spie Vol. 5464 (Spie, Bellingham, Wa, 2004)0277-786x/04/\$15 · Doi: 10.1117/12.544970
- <sup>61</sup> David L. Andrews And Garth A. Jones, "Primary Photonic Processes In Energy Harvesting: Quantum Dynamical Analysis Of Exciton Energy Transfer Over Three-Dimensional Dendrimeric Geometries," Mater. Res. Soc. Symp. Proc. Vol. 1325 © 2011 Materials Research Society. Doi: 10.1557/Opl.2011.846
- <sup>62</sup> Jason Lewis, Jian Zhang, And Xiaomei Jiang, "Fabrication Of Organic Solar Array For Applications In Microelectromechanical Systems," J. Renewable Sustainable Energy 1, 013101 (2009); Doi: 10.1063/1.2998825.
- <sup>63</sup> Jeffrey Peet, Alan J. Heeger, And Guillermo C. Bazan, "Plastic" Solar Cells: Self-Assembly Of Bulk Heterojunction Nanomaterials By Spontaneous Phase Separation" Accounts Of Chemical Research 1700-1708 November 2009 Vol. 42, No. 11; Moon, J. S.; Lee, J. K.; Cho, S.; Byun, J.; Heeger, A. J. "Columnlike" structure of the cross-sectional morphology of bulk heterojunction materials. Nano Lett. 2009, 9, 230–234.
- <sup>64</sup> Bin Liu and Eray S. Aydil Layered mesoporous nanostructures for enhanced light harvesting in dye-sensitized solar cells, Renewable Sustainable Energy 3 , 043106 (2011); doi: 10.1063/1.3615641.
- <sup>65</sup> George Thomas, K.; Kamat, P. V. Chromophore Functionalized Gold Nanoparticles. Acc. Chem. Res. 2003, 36, 888-898.
- <sup>66</sup> Claire Jean-Mistral, C., Carlioz, L., Defosseux, M., Marzencki, M., Cugat, O., Delamare, J., And Basrour, S., "Thermo-Magnetic, Piezo-Electric And Electroactive Energy Harvesting Devices," Mater. Res. Soc. Symp. Proc. Vol. 1218 © 2010 Materials Research Society 1218-Z04-03.
- <sup>67</sup> Maxime Defosseux, Marcin Marzencki And Skandar Basrour, "Piezoelectric Vibration Harvesting Device With Automatic Resonance Frequency Tracking Capability," Mater. Res. Soc. Symp. Proc. Vol. 1218 © 2010 Materials Research Society 1218-Z07-09.

- 
- <sup>68</sup> A Cammarano, S G Burrow, And D A W Barton, "Modelling And Experimental Characterization Of An Energy Harvester With Bi-Stable Compliance Characteristics," *Proceedings Of The Institution Of Mechanical Engineers, Part I: Journal Of Systems And Control Engineering* June 2011 225: 475-484, Doi:10.1177/0959651811403093.
- <sup>69</sup> A J Sneller, P Cette, And B P Mann, "Experimental Investigation Of A Post-Buckled Piezoelectric Beam With An Attached Central Mass Used To Harvest Energy," *Proceedings Of The Institution Of Mechanical Engineers, Part I: Journal Of Systems And Control Engineering* June 2011 225: 497-509, Doi:10.1177/0959651811401954
- <sup>70</sup> M. Li, Y. Wen\*, P. Li, J. Yang, And X. Dai, "A Rotation Energy Harvester Employing Cantilever Beam And Magnetostrictive/Piezoelectric Laminate Transducer," *Sensors And Actuators A* 166 (2011) 102–110.
- <sup>71</sup> L. Wang And Fg Yuan, "Vibration Energy Harvesting By Magnetostrictive Material," *Smart Mater. Struct.* 17 (2008) 045009 (14pp). Doi:10.1088/0964-1726/17/4/045009.
- <sup>72</sup> B.P. Mann, N.D.Sims, "Energy Harvesting from the nonlinearoscillations of Magnetic levitation," *Journal of Sound and Vibration* 319(2009)515–530.
- <sup>73</sup> Min Hyung Lee & Ali Javey, "Electronics: Power Surfing On Waves," *Nature*, 472, Pg: 304–305, April 21<sup>st</sup>, 2011. Doi: Doi:10.1038/472304a.
- <sup>74</sup> Vr Challa, M Prasad, And Ft Fisher, "Towards An Autonomous Self-Tuning Vibration Energy Harvesting Device For Wireless Sensor Network Applications," *Smart Mater. Struct.* 20 (2011) 025004 (11pp). Doi:10.1088/0964-1726/20/2/025004.
- <sup>75</sup> X. Chen, S. Xu, N. Yao, And Y. Shi, "1.6 V Nanogenerator For Mechanical Energy Harvesting Using Pzt Nanofibers," *Nano Lett.* 2010, 10, 2133–2137. Doi: 10.1021/Nl100812k.
- <sup>76</sup> D. Van Gough, A.T. Juhl, And P.V. Braun, "Programming Structure Into 3d Nanomaterials," *Materials Today*, June 2009, Vol. 12, Number 6.
- <sup>77</sup> A.I. Hochbaum, And P. Yang, "Semiconductor Nanowires For Energy Conversion," *Chem. Rev.* 2010, 110, 527–546.
- <sup>78</sup> F.D.S. Marquis, "Carbon Nanotube Nanostructured Hybrid Materials Systems For Renewable Energy Applications," *JOM*, 63 (1), P.48-53, 2011.
- <sup>79</sup> Y. Qi, J. Kim, T.D. Nguyen, B. Lisko, P.K. Purohit, And M.C. Mcalpine, "Enhanced Piezoelectricity And Stretchability In Energy Harvesting Devices Fabricated From Buckled Pzt Ribbons," *Nano Lett.* 2011, 11, 1331–1336. Dx.Doi.Org/10.1021/Nl104412b.
- <sup>80</sup> B. Tian, X. Zheng, T.J. Kempa, Y. Fang, N. Yu, G. Yu, J. Huang and C.M. Lieber, "Coaxial silicon nanowires as solar cells and nanoelectronic power sources," *Nature* 449, 885-890 (2007).
- <sup>81</sup> D.J. Lipomi And Z. Bao, "Stretchable, Elastic Materials And Devices For Solar Energy Conversion," *Energy Environ. Sci.*, 2011, 4, 3314–3328.

- 
- <sup>82</sup> M. Peckerar, Z. Dilli, M. Dornajafi, N. Goldsman, Y. Ngu, R. B. Proctor, B. J. Krupsaw And D. A. Lowy, A novel high energy density flexible galvanic cell *Energy Environ. Sci.*, 2011, 4, 1807.
- <sup>83</sup> H. Gwon, H.-S. Kim, K. U. Lee, D.-H. Seo, Y. C. Park, Y.-S. Lee, B. T. Ahn And K. Kang, Flexible energy storage devices based on graphene paper *Energy Environ. Sci.*, 2011, 4, 1277.
- <sup>84</sup> S. Tominaka, H. Nishizeko, J. Mizuno And T. Osaka, Bendable fuel cells: on-chip fuel cell on a flexible polymer substrate *Energy Environ. Sci.*, 2009, 2, 1074.
- <sup>85</sup> M. Kaltenbrunner, G. Kettlgruber, C. Siket, R. Schwodiauer And S. Bauer, Arrays of Ultracompliant Electrochemical Dry Gel Cells for Stretchable Electronics *Adv. Mater.*, 2010, 22, 2065.
- <sup>86</sup> C. J. Yu, C. Masarapu, J. P. Rong, B. Q. Wei And H. Q. Jiang, Stretchable Supercapacitors Based on Buckled Single-Walled Carbon Nanotube Macrofilms *Adv. Mater.*, 2009, 21, 4793.
- <sup>87</sup> R. Rai, I. Coondoo, R. P. Lopes, I. Bdkin, R. Ayouchi, S. Bhattacharaya, R. Schwarz, A. L. Kholkin, "Development Of Lead-Free Materials For Piezoelectric Energy Harvesting," *Mater. Res. Soc. Symp. Proc. Vol. 1325* © 2011 Materials Research Society. Doi: 10.1557/Opl.2011.847
- <sup>88</sup> Scott Moss, Alex Barry, Ian Powlesland, Steve Galea, And Gregory P. Carman, "A Low Profile Vibro-Impacting Energy Harvester With Symmetrical Stops," *Applied Physics Letters* 97, 234101, 2010.
- <sup>89</sup> Veronica Corral-Flores, Dario Bueno-Baqués, Ronald F. Ziolo, "Hybrid Batio3-Pvdf Piezoelectric Composites For Vibration Energy Harvesting Applications," *Mater. Res. Soc. Symp. Proc. Vol. 1325* © 2011 Materials Research Society. Doi: 10.1557/Opl.2011.1059
- <sup>90</sup> T-W Ma, "Opportunities For Using Non-Linear Oscillators To Enhance Energy Harvesting From Impulsively Loaded Structures," *Proc. ImechE, Part I: J. Systems And Control Engineering*, 225, 2011, 467-474. Doi: 10.1177/2041304110394563.
- <sup>91</sup> R P Simion Ands Sen, "Non-Linear Resonance-Like Processes In Confined Driven Granular Alignments And Energy Harvesting," *Proceedings Of The Institution Of Mechanical Engineers, Part I: Journal Of Systems And Control Engineering* June 2011 225: 522-529, Doi:10.1177/0959651811400940.
- <sup>92</sup> M F Daqaq Andd Bode, "Exploring The Parametric Amplification Phenomenon For Energy Harvesting *Proceedings Of The Institution Of Mechanical Engineers,*" Part I: *Journal Of Systems And Control Engineering*, June 2011 225: 456-466, Doi:10.1177/2041304110401145
- <sup>93</sup> John Lake, Jiyuan Luan, Zuki Tanaka, Bin Liang, And Bin Chen, "Piezoelectric Materials And Devices For Wind Energy Harvesting," *Mater. Res. Soc. Symp. Proc. Vol. 1325* © 2011 Materials Research Society. Doi: 10.1557/Opl.2011.1061
- <sup>94</sup> Giuseppe Vasta, Timothy J. Jackson, James Bowen, And Edward J. Tarte, "New Multilayer Architectures For Piezoelectric Batio3 Cantilever Systems," *Mater. Res. Soc. Symp. Proc. Vol. 1325* © 2011 Materials Research Society, Doi: 10.1557/Opl.2011.970.
- <sup>95</sup> R Ramlan, M J Brennan, And B R Mace, "On The Optimum Parameters Of A Device For Harvesting Energy From Running And Walking," *Proceedings Of The Institution Of Mechanical Engineers, Part I: Journal Of Systems And Control Engineering* June 2011 225: 510-521, Doi:10.1177/0959651811407407.

- 
- <sup>96</sup> A Erturk Andd J Inman, "Parameter Identification And Optimization In Piezoelectric Energy Harvesting: Analytical Relations, Asymptotic Analyses, And Experimental Validations," *Proceedings Of The Institution Of Mechanical Engineers, Part I: Journal Of Systems And Control Engineering* June 2011 225: 485-496, Doi:10.1177/0959651810396280.
- <sup>97</sup> Jong-Hyeon Jeong, Chiharu Kimura, Hidemitsu Aoki, Masanori Okuyama And Takashi Sugino, "Thin Film Formed By Annealing Process With Electric Field," 2009 Mrs Fall Meeting.
- <sup>98</sup> I. Karaman, B. Basaran, H.E. Karaca, A. I. Karsilayan, And Y. I. Chumlyakov, "Energy Harvesting Using Martensite Variant Reorientation Mechanism In A Nimnga Magnetic Shape Memory Alloy," *Applied Physics Letters* 90, 172505 2007.
- <sup>99</sup> H. Zhang, "Power Generation Transducer From Magnetostrictive Materials," *Applied Physics Letters* 98, 232505-1, 2011.
- <sup>100</sup> Shuxiang Dong, Junyi Zhai, J. F. Li, D. Viehland, And S. Priya, "Multimodal System For Harvesting Magnetic And Mechanical Energy," *Appl. Phys. Lett.* 93, 103511-3, 2008.
- <sup>101</sup> D. Spreemann, Y. Manoli, B. Folkmer, D. Mintenbeck, Non-resonant vibration conversion, *J. Micromech. Microeng.* 16 (2006) 169–173.
- <sup>102</sup> X.Z. Dai, Y.M. Wen, P. Li, J. Yang, X.F. Jiang, A vibration energy harvester using Magnetostrictive/Piezoelectric composite transducer, *Proc. IEEE sensors* 156 (2009) 1450–1477.
- <sup>103</sup> X.Z. Dai, Y.M. Wen, P. Li, J. Yang, G.Y. Zhang, Modeling, characterization and fabrication of vibration energy harvester using Terfenol-D/PZT/Terfenol-D composite transducer, *J. Sens. Actuators A: Phys.* 156 (2009) 350–358.
- <sup>104</sup> P. T. Eubank, M. R. Patel, M. A. Barrufet, and B. Bozkurt, *J. Appl. Phys.* 73, 4104 ~1993.
- <sup>105</sup> A. E. Berkowitz and J. L. Walter, *J. Mater. Res.* 2, 277 ~1987.
- <sup>106</sup> R. H. Kodama, A. E. Nash, F. E. Spada, and A. E. Berkowitz, *Nanophase Materials* ~Kluwer Academic, Dordrecht, Netherlands, 1994!, p. 101.
- <sup>107</sup> A. E. Berkowitz, H. Harper, David J. Smith, Hao Hu, Qian Jiang, and Virgil C. Solomon and H.B. Radousky, "Hollow Metallic Microspheres Produced by Spark Erosion", *Applied Physics Letters*, 85, 940, 2004..
- <sup>108</sup> J. Carrey, H.B. Radousky, A.E. Berkowitz, Spark-eroded Particles: Influence of Processing Parameters. *Journal of Applied Physics*, 95, 823.
- <sup>109</sup> Nersesse Nersessian, Siu Wing Or, Gregory P. Carman, Wonyoung Choe, And Harry B. Radousky, "Hollow And Solid Spherical Magnetostrictive Particulate Composites," *Citation: J. Appl. Phys.* 96, 3362 (2004); Doi: 10.1063/1.1775303.
- <sup>110</sup> Gao, Y.; Wang, Z. L. *Nano Lett.* 2007, 7, 2499–2505.

---

<sup>111</sup> Yue-Guang Deng and Jing Liu Recent advances in direct solar thermal power generation, J. Renewable Sustainable Energy 1, 052701 (2009); doi: 10.1063/1.3212675

<sup>112</sup> D. H. Hecht, U.S. Patent No. US2007289622-A1 December 20, 2007.

<sup>113</sup> Adrian Koh, A., "Maximum Energy That Can Be Harvested From A Dielectric Elastomer Generator," Mater. Res. Soc. Symp. Proc. Vol. 1218 © 2010 Materials Research Society 1218-Z07-10.

<sup>114</sup> P. Choi, N. H. Jalani, And R. Datta, "Thermodynamics And Proton Transport In Nafion li. Proton Diffusion Mechanisms And Conductivity," Journal Of The Electrochemical Society, Vol. 152 (3), E123-E130, 2005.

<sup>115</sup> Michael Freunek, Monika Müller, Tolgay Ungan, William Walker, and Leonhard M. Reindl New Physical Model For Thermoelectric Generators Journal Of Electronic Materials, Vol. 38, No. 7, 2009 Doi: 10.1007/S11664-009-0665-Y

<sup>116</sup> Trinh T.M. Vo, Andrew J. Williamson, Vincenzo Lordi, Giulia Galli Atomistic Design of Thermoelectric Properties of Silicon Nanowires Nano Lett., 2008, 8 (4), pp 1111–1114 DOI: 10.1021/nl073231d

<sup>117</sup> Denis O Demchenko<sup>1\*</sup>, Peter D Heinz<sup>2</sup> and Byounghak Lee<sup>2</sup>Determining factors of thermoelectric properties of semiconductor nanowires Nanoscale Research Letters 2011, 6:502

<sup>118</sup> M. Shelley and A. A. Mostofi Prediction of high  $zT$  in thermoelectric silicon nanowires with axial germanium heterostructures EPL, 94 (2011) 67001 www.epljournal.org doi: 10.1209/0295-5075/94/67001

<sup>119</sup> Jani Oksanen And Jukka Tulkki, "A Thermophotonic Heat Pump/Heat Engine," Mater. Res. Soc. Symp. Proc. Vol. 1218 © 2010 Materials Research Society, 1218-Z07-01.